



RESEARCH ARTICLE SUMMARY

BICCN

Signature morphoelectric properties of diverse GABAergic interneurons in the human neocortex

Brian R. Lee* and Rachel Dalley* et al.

INTRODUCTION: Recent studies using single-cell transcriptomic analysis have shed new light on genetically defined cell types in the human brain. However, a deeper understanding of multimodal cellular properties, such as electrical activity and morphology, remains elusive and is central to understanding the role of distinct cell types in cognitive function and disease.

RATIONALE: Understanding the fundamental properties of different cell types is important for gaining insights into their role in neural circuits, cognition, and disease. This is challenging for cell types in the human brain because of the limited availability of tissue, the heterogeneity of neurons, and the lack of genetic approaches to effectively target these spatially distributed and in some cases, exceedingly rare types. Rapid viral genetic labeling and patch-clamp electrophysiology combined with RNA sequencing (Patch-seq) facilitates the targeting of specific cell types in tissue from human neurosurgeries and thus allows the characterization of multimodal properties of neurons in the human cortex.

RESULTS: Patch-seq sampling facilitated targeted acquisition and analysis of 778 human neurons in cortical layers 2 to 6, across 44 out of 45 γ -aminobutyric acid-producing (GABAergic) transcriptomic types. Aggregated data from acute and culture paradigms provide new descriptions and direct comparison of the signature morphoelectric properties of the canonical human interneuron subclasses, LAMP5/PAX6, VIP, SST, and PVALB, and a deeper dive into features of select GABAergic transcriptomic types.

Detailed characterization of the SST subclass revealed specific multimodal properties of individual transcriptomic types. The SST FRZB transcriptomic type exhibits gene expression signatures along a continuum of PVALB and SST subclasses, but the morphoelectric properties of this type clearly indicate strong alignment with the PVALB subclass. For an additional transcriptomic type, SST CALB1, we found multiple discrete morphological types suggesting that further splitting may be warranted. Double-bouquet cells of the human neocortex belong to two transcriptomic types within the SST subclass with enrichment in temporal versus

frontal cortex regions. We compared the morphoelectric properties of homologous mouse and human neocortical GABAergic neuron types and found that human types are more excitable and have a larger spatial extent with less neurite branching.

CONCLUSION: An impactful finding of our study is the direct demonstration of how multimodal Patch-seq data is vital to refinement of transcriptomic cell-type taxonomies. Cellular taxonomies built on single-cell transcriptomes and differential gene expression are not static but rather represent a starting foundation to build upon as new data modalities are obtained and aligned at the resolution of transcriptomic types. We also demonstrate the immense potential and utility of viral genetic labeling and Patch-seq for targeted analysis of human neocortical GABAergic neuron subclasses and types in ex vivo brain slices. This work can serve as a roadmap for future functional studies of human brain cell types at the resolution of emerging transcriptomic cell-type taxonomies and provides a rich open-access dataset for exploring gene-function relationships for a wide diversity of human neocortical GABAergic neuron types. ■

The list of author affiliations is available in the full article online.

*These authors contributed equally to this work.

Corresponding author. Email: edl@alleninstitute.org (E.S.L.); jonathan@alleninstitute.org (J.T.T.)

Cite this article as B. R. Lee et al., *Science* **382**, eadf6484 (2023). DOI: 10.1126/science.adf6484

S READ THE FULL ARTICLE AT
<https://doi.org/10.1126/science.adf6484>

Patch-seq analysis of human GABAergic neurons.

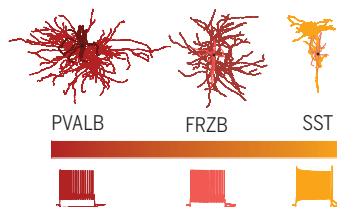
(A) MRIs are obtained to accurately map the area of resected human brain tissue. (B) Viral labeling combined with Patch-seq is used to collect the multimodal properties of human cortical GABAergic neurons. Each sample is mapped to a taxonomy to identify the transcriptomic type. (C) Representative GABAergic subclasses, their morphologies, and action-potential firing patterns.

(D) Transcriptomic type SST FRZB is found along a continuum of electrophysiological and morphological features between the SST and PVALB subclasses. (E) Morphologically defined double-bouquet cells map to both SST CALB1 and SST ADGRG6, each displaying a distinct distribution across the cortical layers. (F) Homology mapping of PVALB types between mice and humans reveals morphological and electrophysiological differences, including larger spatial extent and higher excitability of human neurons.

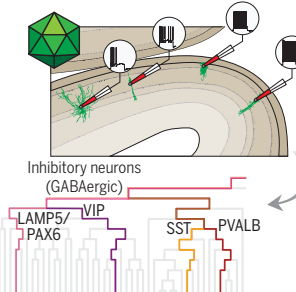
A MRI delineating region of neurosurgical resected brain tissue



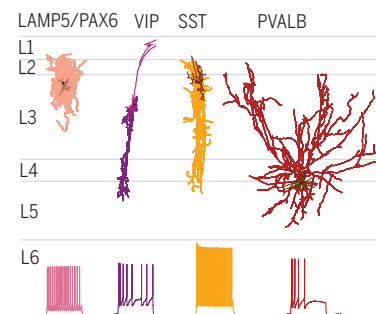
D Alignment of SST FRZB neurons with PVALB subclass



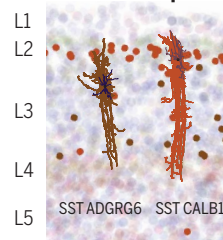
B Viral labeling and Patch-seq multimodal data collection



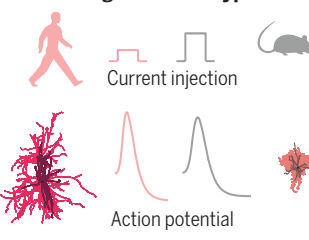
C GABAergic subclass mapping



E Transcriptomic identity of double bouquet cells



F Species differences in a homologous PVALB type



RESEARCH ARTICLE

BICCN

Signature morphoelectric properties of diverse GABAergic interneurons in the human neocortex

Brian R. Lee^{1†}, Rachel Dalley^{1†}, Jeremy A. Miller¹, Thomas Chartrand^{1,2}, Jennie Close¹, Rusty Mann¹, Alice Mukora¹, Lindsay Ng¹, Lauren Alfiler¹, Katherine Baker¹, Darren Bertagnolli¹, Krissy Brouner¹, Tamara Casper¹, Eva Csajbok³, Nicholas Donadio¹, Stan L.W. Driessens⁴, Tom Eggdorff¹, Rachel Enstrom¹, Anna A. Galakhova⁴, Amanda Gary¹, Emily Gelfand¹, Jeff Goldy¹, Kristen Hadley¹, Tim S. Heistek⁴, Dijon Hill¹, Wen-Hsien Hou⁵, Nelson Johansen¹, Nik Jorstad¹, Lisa Kim^{1,2}, Agnes Katalin Kocsis³, Lauren Kruse¹, Michael Kunst¹, Gabriela León¹, Brian Long¹, Matthew Mallory¹, Michelle Maxwell¹, Medea McGraw¹, Delissa McMullen¹, Erica J. Melief⁶, Gabor Molnar³, Marty T. Mortrud¹, Dakota Newman¹, Julie Nyhus¹, Ximena Opitz-Araya¹, Attila Ozsvár⁵, Trangthan Pham¹, Alice Pom¹, Lydia Potekhina¹, Ram Rajanbabu¹, Augustin Ruiz¹, Susan M. Sunkin¹, Ildikó Szöts³, Naz Taskin¹, Bargavi Thyagarajan¹, Michael Tieu¹, Jessica Trinh¹, Sara Vargas¹, David Vumbaco¹, Femke Waleboer⁴, Sarah Walling-Bell¹, Natalie Weed¹, Grace Williams¹, Julia Wilson¹, Shengqin Yao¹, Thomas Zhou¹, Pál Barzó⁷, Trygve Bakken¹, Charles Cobbs⁸, Nick Dee¹, Richard G. Ellenbogen⁹, Luke Esposito¹, Manuel Ferreira⁹, Nathan W. Gouwens¹, Benjamin Grannan⁹, Ryder P. Gwinn⁸, Jason S. Hauptman⁹, Rebecca Hodge¹, Tim Jarsky¹, C. Dirk Keene⁶, Andrew L. Ko⁹, Anders Rosendal Korshoej¹⁰, Boaz P. Levi¹, Kaare Meier^{10,11}, Jeffrey G. Ojemann⁹, Anoop Patel⁹, Jacob Ruzevick⁹, Daniel L. Silbergeld⁹, Kimberly Smith¹, Jens Christian Sørensen^{10,12}, Jack Waters^{1,13}, Hongkui Zeng¹, Jim Berg^{1,2}, Marco Capogna⁵, Natalia A. Goriounova⁴, Brian Kalmbach^{1,13}, Christiaan P.J. de Kock⁴, Huib D. Mansvelder⁴, Staci A. Sorenson¹, Gabor Tamas³, Ed S. Lein^{1,9*}, Jonathan T. Ting^{1,13*}

Human cortex transcriptomic studies have revealed a hierarchical organization of γ -aminobutyric acid-producing (GABAergic) neurons from subclasses to a high diversity of more granular types. Rapid GABAergic neuron viral genetic labeling plus Patch-seq (patch-clamp electrophysiology plus single-cell RNA sequencing) sampling in human brain slices was used to reliably target and analyze GABAergic neuron subclasses and individual transcriptomic types. This characterization elucidated transitions between PVALB and SST subclasses, revealed morphological heterogeneity within an abundant transcriptomic type, identified multiple spatially distinct types of the primate-specialized double bouquet cells (DBCs), and shed light on cellular differences between homologous mouse and human neocortical GABAergic neuron types. These results highlight the importance of multimodal phenotypic characterization for refinement of emerging transcriptomic cell type taxonomies and for understanding conserved and specialized cellular properties of human brain cell types.

Recent work on the human brain has shed light on transcriptomic cell type diversity, including the identification of previously undescribed cell types and finer distinctions than previously recognized (1–11). However, a deeper understanding of the phenotypic properties of transcriptomic types is necessary to provide mechanistic insights into their role in cognitive function and disease. Although it is hypothesized in transcriptomic type classification that differentially expressed genes within each transcriptomic type underlie distinct morphological and functional properties, direct measurements are lagging well behind the pace of transcriptomic characterization. Additionally, there exists unresolved ambiguity across, and diversity within, transcriptomic types that remain underexplored for many different brain regions and species.

The Patch-seq method (patch-clamp electrophysiology plus single-cell RNA sequencing) provides the most direct means to determine

the fundamental morphoelectric properties of neuronal transcriptomic types, evaluate distinctness between types, and explore gene-function relationships (12–14). Recently, this approach has been used successfully to characterize the most abundant glutamatergic pyramidal neuron types in the human supragranular cortex (15). This work provided a deep functional context regarding the expanded diversity of human glutamatergic pyramidal neuron types relative to those of the mouse supragranular cortex, as well as the elucidation of the transcriptomic identity of human cortical cell types with selective vulnerability in disease. Additionally, gradients in gene expression were largely mirrored by gradients in other measured morphoelectric features, consistent with other recent Patch-seq studies of mouse cortical neuron types (16, 17). The Patch-seq technique has also been used to measure the multimodal cellular properties of cortical layer 5 extratelencephalic-projecting (L5 ET) neurons

in the human cortex and to apply homology mapping based on analysis of single-cell transcriptomes for comparing the cellular features of this subcortically projecting cortical neuron type across mammalian species (18).

γ -aminobutyric acid-producing (GABAergic) neurons are crucial for modulating and tuning neuronal circuits (19) and their dysfunction is at the forefront of a variety of human brain disorders (20–22), yet a comprehensive characterization of human cortical GABAergic neuron types has proven technically far more challenging. This stands in contrast to decades of impressive advances in the mouse model, where development and refinement of a multitude of viral and transgenic targeting and *in vivo* perturbation strategies have facilitated rapid progress (23). GABAergic neurons in the cortex historically have been subdivided into four major subclasses based on the neurochemical markers they express: parvalbumin (PVALB), somatostatin (SST), vasoactive intestinal peptide (VIP), and LAMP5/PAX6 [synonymous with 5-hydroxytryptamine receptor 3A (HTR3A)-expressing, but lacking VIP] (23, 24). Single-cell transcriptomics studies of the mouse and human cortex revealed previously unrecognized diversity of neuron types within each of these four canonical interneuron subclasses (1, 25, 26). Mouse Patch-seq studies of cortical GABAergic neurons have shown discrete morphological and electrophysiological properties between the subclasses, yet a continuum within each subclass (16, 17).

By comparison, similar studies of the human cortex have proven challenging owing to the limited availability of adult human brain tissue and lack of genetic approaches to effectively target these spatially distributed, and in some cases, exceedingly rare types. Prior single-neuron electrophysiology studies of human cortical GABAergic neurons are relatively few and have relied mainly on firing patterns, such as fast spiking (FS) versus non-FS, limited marker genes, or gene panels to achieve approximate

¹Allen Institute for Brain Science, Seattle, WA 98109, USA.

²Allen Institute for Neural Dynamics, Seattle, WA 98109, USA.

³MTA-SZTE Research Group for Cortical Microcircuits, Department of Physiology, Anatomy, and Neuroscience, University of Szeged, 6726 Szeged, Hungary. ⁴Department of Integrative Neurophysiology, Center for Neurogenomics and Cognitive Research (CNCR), Vrije Universiteit, Amsterdam, 1081 HV, Netherlands. ⁵Department of Biomedicine, Aarhus University, 8000 Aarhus, Denmark. ⁶Department of Laboratory Medicine and Pathology, University of Washington, Seattle, WA 98195, USA. ⁷Department of Neurosurgery, University of Szeged, 6725 Szeged, Hungary.

⁸Swedish Neuroscience Institute, Seattle, WA 98122, USA.

⁹Department of Neurological Surgery, University of Washington, Seattle, WA 98195, USA. ¹⁰Department of Neurosurgery, Aarhus University Hospital, 8200 Aarhus, Denmark. ¹¹Department of Anesthesiology, Aarhus University Hospital, 8200 Aarhus, Denmark. ¹²Center for Experimental Neuroscience, Aarhus University Hospital, 8200 Aarhus, Denmark. ¹³Department of Physiology and Biophysics, University of Washington, Seattle, WA 98195, USA.

*Corresponding author. Email: edl@alleninstitute.org (E.S.L.); jonathan@alleninstitute.org (J.T.T.).

†These authors contributed equally to this work.

alignment to subclasses described in rodents (3, 27–33). The previous lack of a comprehensive human cortical cell-type taxonomy as a reference for these studies likely hindered efforts at classification, and the degree of conservation between human and mouse neocortical GABAergic cell-type diversity and marker-gene expression has only partially been delineated. Here we combined rapid viral genetic labeling with Patch-seq in cortical slices derived from human neurosurgical resections. Mapping of recorded neurons to transcriptomically defined types in our human cortical taxonomy facilitated a detailed functional annotation of human neocortical GABAergic subclasses and select abundant transcriptomic types.

Results

We performed Patch-seq experiments to characterize the electrophysiological, morphological, and transcriptomic profiles of GABAergic neurons in human neocortical brain slices using a well-established Patch-seq platform (13–15). To expand our sampling capability, both temporally and to facilitate preferential targeting with viral genetic labeling, we implemented a human ex vivo brain slice culture paradigm (34). Brain slices were transduced with an adeno-associated virus (AAV) vector CN1390 that has been shown to fluorescently label human cortical GABAergic neurons across all four canonical GABAergic subclasses (35), which enabled direct visualization and targeting for Patch-seq experiments (Fig. 1A) (2, 35).

We obtained human samples from neurosurgically resected neocortical tissues and processed them with standardized protocols across three experimental sites in the U.S., the Netherlands, and Hungary (14, 15, 18, 36); most samples originated from the temporal and frontal lobes (data S1). Human Patch-seq neurons were mapped to a middle temporal gyrus (MTG) single-nucleus transcriptomics-based reference taxonomy (1) and assigned to a transcriptomic subclass and type by using a “tree-mapping” classifier (materials and methods) (16).

Morphological, electrophysiological, and transcriptomic features in the slice culture paradigm

With the use of Patch-seq recordings, we examined the acute and culture brain slice paradigms with three different data modalities: transcriptome, morphology, and electrophysiology. Patch-seq neurons from culture preparations recorded at 2 to 16 days in culture (DIC) had significantly ($P < 0.0001$) higher genes detected as compared with the acute paradigm (Fig. 1B). This elevation was prevalent and remained consistent across all days sampled in culture (fig. S1A). Recent work has shown that Patch-seq samples may exhibit elevated microglial marker genes (37); therefore,

we sought to determine if the increased number of genes observed in the culture paradigm was specific to microglial markers. We performed standard Seurat V4 clustering on Patch-seq neurons from the culture paradigm (38). These neurons clustered into two domains, with or without microglial gene expression signatures, indicating that more variation was explained by microglial than by cell type-associated genes (fig. S1B). This microglial signature (data S2) was also observed in a subset of neurons collected with the acute paradigm, although the effect was less pronounced (fig. S1, B and C). Microglial gene signatures did not impact the ability to accurately map transcriptomic types, as neurons of the same subclass defined from tree mapping colocalized when visualizing the transcriptome through a uniform manifold approximation projection (UMAP) (39), either when integrating by paradigm and microglial signature (fig. S1D) or when restricting the analysis only to marker genes (fig. S1E). Upon examination of key differentially expressed genes responsible for GABAergic subclass discrimination, average gene expression was strongly correlated ($P < 0.0001$), demonstrating alignment between acute and culture paradigms (Fig. 1C). Collectively, when examining the normalized marker sum (NMS) score, a method to quantify the expression of mapping-related marker genes (14, 40), we found no difference between the acute and culture paradigms (Fig. 1D). These results suggest that the key markers used to map cell types are not perturbed in the culture paradigm or in the presence of microglial signatures, thereby allowing accurate mapping of transcriptomic types.

To further examine differences between Patch-seq in acute and cultured slices, we performed an in-depth investigation into the most abundant type, L2-4 PVALB WFDC2 (hereafter called PVALB WFDC2). For this transcriptomic type, the acute and culture datasets exhibited overlap in transcriptomic UMAP space (Fig. 1E). We also evaluated 50 morphological features of cortical depth-matched PVALB WFDC2 neurons (Fig. 1F) from culture ($n = 9$) and acute paradigms ($n = 10$) and didn't find any difference among the two conditions (fig. S2A). Additionally, dimensionality reduction of the morphological features showed that PVALB WFDC2 neurons from the culture and acute paradigms occupied similar space in the PVALB-rich portion of morphological UMAP, demonstrating consistency in the morphometric features between the two paradigms (Fig. 1H).

Analysis of electrophysiological responses from PVALB WFDC2 neurons revealed that 43 of 84 features differed across the two paradigms (fig. S2B). Overlaid voltage traces of a single action potential (AP) and response to hyperpolarizing current are shown in Fig. 1, J and K, respectively. AP width and sag are two of the key features that were different between

the two groups (Fig. 1L); however, multiple other cardinal intrinsic membrane properties, such as interspike interval or input resistance, were not. When projecting all 84 electrophysiological features through the UMAP, PVALB WFDC2 neurons from both paradigms occupied a similar space (Fig. 1I). The features that were different between the two paradigms were observed at the earliest time point (2 DIC) and did not change with additional days in culture (fig. S2C). With the increase in gene expression and differences in electrophysiological features in the culture paradigm, we sought to determine if the genes responsible for physiology were preserved or altered. We examined 114 voltage-gated ion-channel genes and found only seven that were different in culture versus acute paradigm (fig S2D).

Comparison of features across human GABAergic subclasses

To achieve a more comprehensive multimodal analysis, we combined the data from acute and culture paradigms and characterized the transcriptomic, intrinsic physiological, and/or morphological properties of 778 neurons from the four canonical GABAergic subclasses in human cortex. We described neurons in cortical layers 2 to 6 (L2–6) across 44 transcriptomic types (fig. S3). When visualized in Seurat-aligned transcriptomic space through UMAP, the Patch-seq dataset overlapped with single-nucleus RNA sequencing (snRNA-seq) human MTG dataset (1), demonstrating the feasibility, consistency, and accuracy of mapping quality (Fig. 2A). PVALB, SST, VIP, and LAMP5/PAX6 interneurons were separable when visualized by electrophysiological (Fig. 2B) and morphological (Fig. 2C) features in UMAP space, with PVALB neurons occupying the most distinct subregions in both UMAPs. Proximity in the UMAPs suggest that quantitative features from all three modalities can be used to distinguish GABAergic subclasses.

Dendrites and axons of a subset of neurons ($n = 140$) with sufficient labeling were imaged at high resolution and digitally reconstructed (Fig. 2D and fig. S4). Neurons from the LAMP5/PAX6 subclass were dominated by classic neurogliaform morphologies, and although found in all cortical layers, here we report predominately on neurons in L2 and L3 [see (36) for an in-depth L1 investigation]. LAMP5/PAX6 neurons were distinguished by their stellate dendrites, numerous primary dendrites, and extensive axon branching. They also had the shortest soma-to-branch tip Euclidean distance for both axon and dendrite (Fig. 2E). The morphological dataset for the VIP subclass, also dominated by neurons in L2 and L3, displayed more diverse morphologies, many with bipolar dendrites and descending axon, with either a wide or narrow profile. To improve sampling of the VIP subclass, we additionally

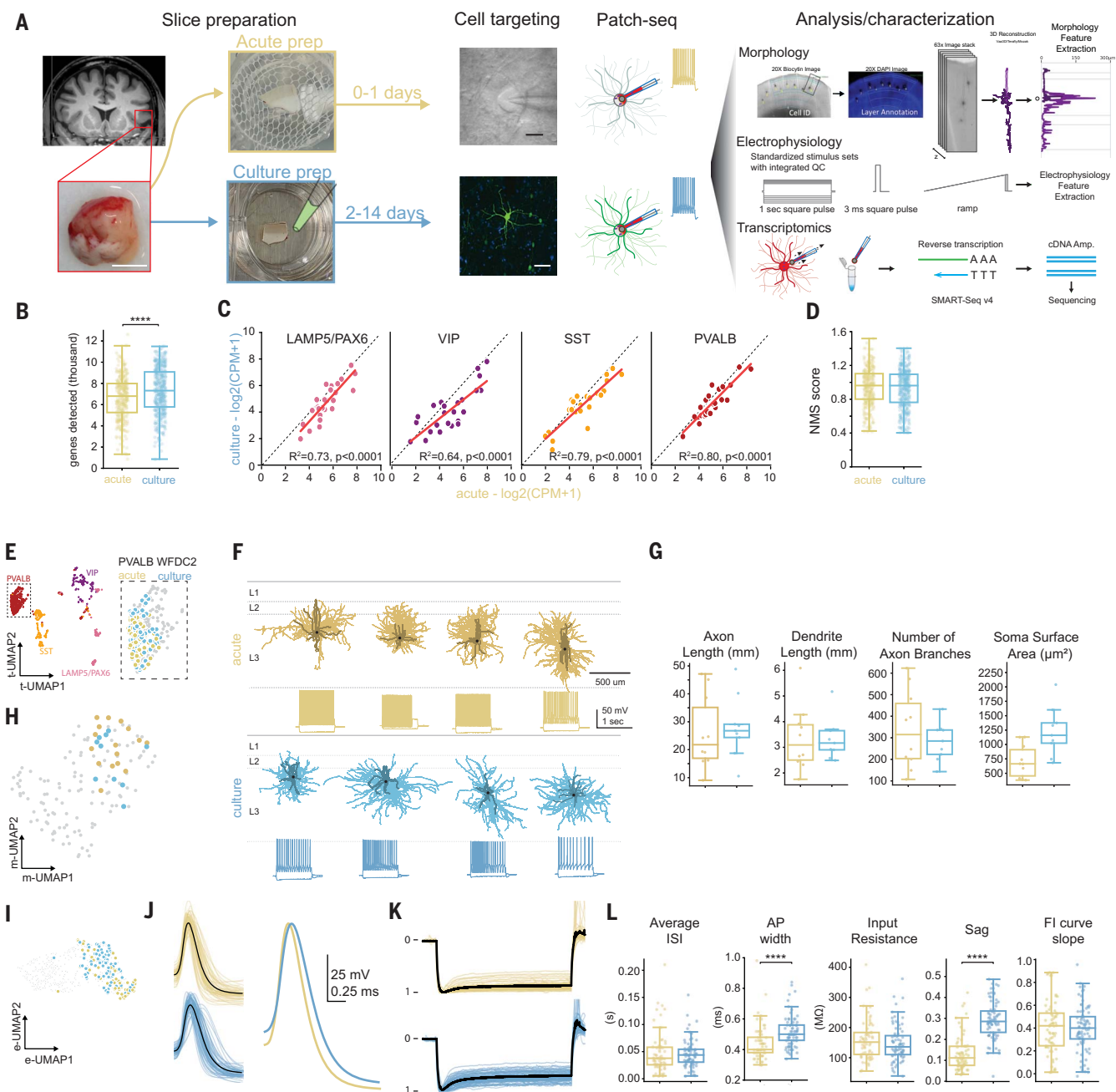


Fig. 1. Slice culture paradigm and multimodal characterization of human cortical GABAergic neurons. (A) Tissue processing schematic for acute and culture paradigm, Patch-seq targeting guided by brightfield or fluorescence, and subsequent multimodal analysis or characterization. Scale bars: human brain specimen, 500 μm ; brightfield of patched neuron, 10 μm ; fluorescent image, 50 μm . (B) Box plot represents the difference in the number of genes detected between the two paradigms. Asterisks indicate significant pairwise comparisons ($****P < 0.0001$, FDR-corrected Mann-Whitney test). (C) Scatter plot of the average gene expression in acute versus culture for the top 25 differentially expressed genes for the LAMP5/PAX6, VIP, SST, and PVALB subclasses. Red line is regression line in each plot. (D) Box plot representing the difference in NMS score between the two paradigms. There were no significant pairwise comparisons (FDR-corrected Mann-Whitney test). (E) UMAP representation of the PVALB-subclass transcriptomic space with PVALB WFDC2 acute and culture neurons highlighted. (F) Cortical depth-matched PVALB WFDC2 morphologies from acute and culture shown aligned to an average cortical

template, with corresponding voltage responses to a 1 s-long current step of -90 pA and rheobase $+80$ pA. (G) Box plots showing select morphology features for cortical depth-matched PVALB WFDC2 neurons from the acute and culture paradigm. There were no significant pairwise comparisons (FDR-corrected Mann-Whitney test). (H) UMAP representation of morphology space with PVALB WFDC2 acute and culture neurons highlighted. (I) UMAP representation of electrophysiology space with PVALB WFDC2 acute and culture neurons highlighted. (J) Overlaid single action potential sweeps from acute and culture PVALB WFDC2 neurons. Black lines represent the mean and are overlaid to the right for direct comparison. (K) Overlaid and normalized voltage response to a -90 pA hyperpolarizing current step from acute and culture PVALB WFDC2 neurons. Black lines represent the mean of the group. (L) Box plots showing select distinguishing features from PVALB WFDC2 neurons from the acute and culture paradigm. Asterisks indicate significant pairwise comparisons ($****P < 0.0001$, FDR-corrected Mann-Whitney test). ISI, interspike interval; FI curve slope, frequency-current curve slope.

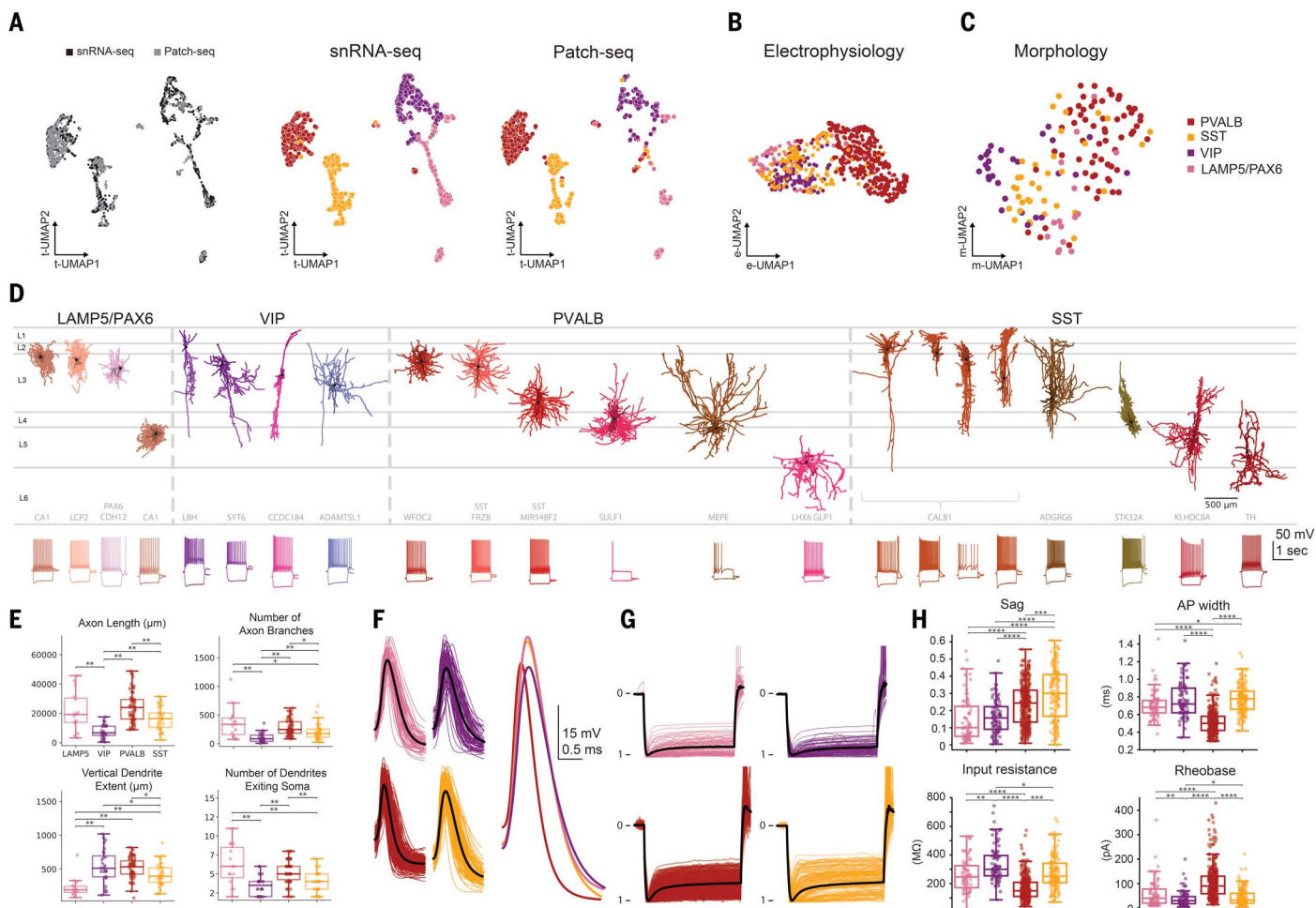


Fig. 2. Human neocortical GABAergic neuron subclass characterization

(A) Integrated snRNA-seq and Patch-seq transcriptomic UMAP of GABAergic neurons. UMAP representations of **(B)** electrophysiology and **(C)** morphology space. **(D)** Representative morphologies from GABAergic subclasses with each transcriptomic type (t-type) represented by different colors and the corresponding t-type gene names (primary t-type gene name representing subclass removed for clarity) displayed in gray at bottom. The morphologies are aligned to an average cortical template with corresponding voltage responses to a 1 s-long current step to a -90 pA and rheobase +80 pA, shown below. **(E)** Box plots representing distinguishing morphology features by

applied an enhancer AAV vector CN2039 to label human neocortical VIP types over other GABAergic neuron subclasses (materials and methods). Although the viral-labeled neurons recorded by Patch-seq did not exclusively map to VIP types, we found strong enrichment for diverse VIP neuron types with small cell bodies and bipolar dendrites in L2 and L3 (fig. S5). The PVALB subclass contained basket cell-like morphologies with multipolar dendrites and radially arrayed axons with a wide horizontal span. The L4-5 MEPE type within the PVALB subclass (Fig. 2D) had axons that spanned L3 to L4 and resembled mouse cortical interlaminar or translaminar basket cells (*16, 41*). The SST subclass contained diverse morphologies with distinct axonal shape. Qualitatively, these morphological types ranged from clas-

sical DBCs to non-Martinotti cells (MCs). One human SST transcriptomic type described in (1) is L4-5 SST STK32A and its corresponding mouse homologs, Sst Hpse Cbln4 and Sst Hpse Sema3c. L4-5 SST STK32A and Sst Hpse Cbln4 shared similar morphological qualities, including being found predominately in L4 and L5 and extensive axonal branching that strongly innervated L4 (16, 42) (Fig. 2D). Mouse Sst Hpse Cbln4 neurons exhibit distinct electrophysiological properties, referred to as quasi fast spiking (16, 43, 44) and preferentially target L4 pyramidal neurons (16, 43, 44), further suggesting that the human homolog L4-5 SST STK32A may also have selective connectivity to L4 pyramidal neurons.

Comprehensive analysis of the associated voltage traces for the four GABAergic subclasses.

subclass (Kruskal-Wallis ANOVA on ranks; $P < 0.05$, FDR corrected. Post-hoc Dunn's test; $*P < 0.05$, $**P < 0.01$, FDR corrected). (F) Overlaid single action potential sweeps from each GABAergic subclass. Black lines represent the mean and are overlaid to the right for direct comparison. (G) Overlaid and normalized voltage response to a 1-s -90-pA hyperpolarizing current step from each GABAergic subclass. Black lines represent the mean of the group. (H) Box plots representing key distinguishing electrophysiological features by subclass (Kruskal-Wallis ANOVA on ranks; $P < 0.05$, FDR corrected. Post-hoc Dunn's test; $*P < 0.05$, $**P < 0.01$, $***P < 0.001$, $****P < 0.0001$, FDR corrected).

LAMP5/PAX6 ($n = 75$), VIP ($n = 99$), SST ($n = 149$), and PVALB ($n = 352$), revealed distinct passive and active electrophysiological features (Fig. 2, B, D, and F to H), consistent with previous rodent studies (23, 45). Example hyperpolarizing and depolarizing voltage traces are shown below the reconstructions in Fig. 2D and demonstrate diversity in intrinsic firing across the interneuron subclasses, which ranges from adapting to irregular or fast spiking. Figure 2F (right) shows overlaid normalized voltage traces of a single AP in response to a current pulse with subclass average. APs from PVALB subclass had the fastest kinetics, whereas LAMP5/PAX6 had the highest peak amplitude versus other subclasses. Overlaid, normalized voltage traces in response to hyperpolarizing current (Fig. 2G) show that LAMP5/PAX6 and VIP subclasses

had minimal sag compared with PVALB and SST subclasses. Several additional features further demonstrated the electrophysiological distinctness of each subclass (Fig. 2H).

Revising subclass assignment based on multimodal data

SST and PVALB subclasses of neocortical GABAergic neurons are known to arise developmentally from the medial ganglionic eminence (10, 24, 46). Whereas most neurons from these subclasses are distinct, neurons from some of the finer transcriptomic types in both mice (26) and humans (7) have gene expression profiles partially consistent with both SST and PVALB subclasses. We examined one such type, L2-4 SST FRZB (hereafter called SST FRZB), and explored its assignment to either the SST or PVALB subclass. We analyzed snRNA-seq data to identify the top 20 differentially expressed genes for the SST and PVALB subclasses and plotted expression in representative neurons from all SST and PVALB transcriptomic types. Whereas neurons belonging to the SST FRZB transcriptomic type did express SST higher than PVALB, they lacked

expression of multiple key genes that define each subclass. However, they expressed multiple other key genes that define each subclass (Fig. 3A), confirming that assignment of this transcriptomic type to SST or PVALB subclass depends on the marker genes selected. Given the intermediate nature of the SST FRZB gene expression signatures, we sought to gain a better understanding of the phenotypic properties of this transcriptomic type that exists along a continuum of the PVALB and SST subclasses.

We took advantage of the multimodal approach of Patch-seq to examine how the phenotypic properties of SST FRZB are related to PVALB and SST subclasses. First, we observed that the vast majority of SST FRZB samples localized to the PVALB subclass within the transcriptomic UMAP space in our Patch-seq dataset (Fig. 3B), consistent with the localization of neurons from the snRNA-seq data in previous work (36). Phenotypically, SST FRZB neurons resembled mostly the PVALB subclass. Examination of all 84 electrophysiological features, visualized using a UMAP, revealed that most

of the SST FRZB neurons colocalized with the PVALB subclass (Fig. 3C). One defining feature of cortical PVALB interneurons is their fast-spiking behavior and narrow APs (16, 47, 48). We observed the AP kinetics, such as upstroke/downstroke ratio, AP width, and AP firing pattern of SST FRZB neurons aligned with fast-spiking interneurons of the PVALB subclass (Fig. 3, D, E, and I). Additionally, these select features of the SST subclass were not different in recordings from acute versus culture paradigms (fig. S6).

Next, we investigated the morphological properties of SST FRZB neurons and found a better overlap with PVALB than with other SST neurons (Fig. 3F). Morphological features such as horizontal axon extent and a measure of the dissimilarity of the axon and dendrite compartments (axon versus dendrite earth mover's distance) showed that SST FRZB neurons had individual morphological features that were more similar to PVALB basket cells than to SST neurons (Fig. 3G). To test whether SST FRZB neurons would align with PVALB basket cells in an unbiased way, we performed hierarchical

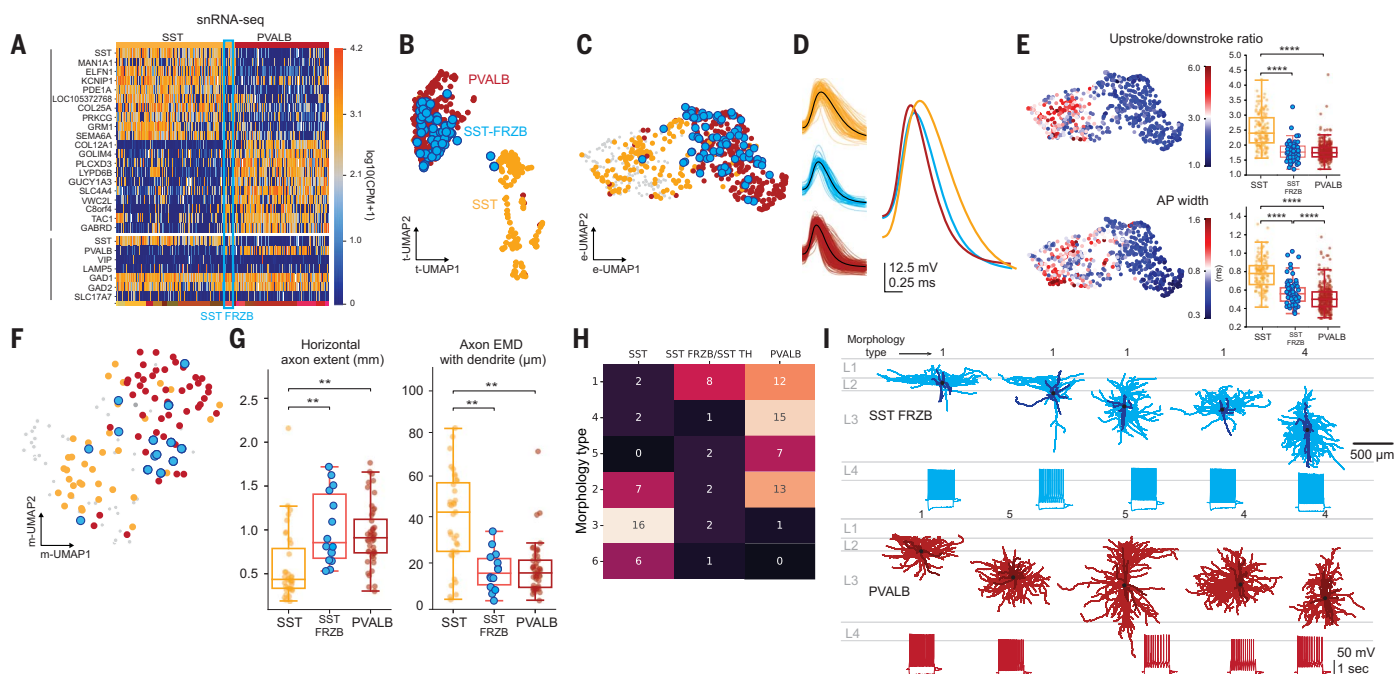


Fig. 3. Phenotypic alignment of SST FRZB neurons with PVALB subclass.

(A) Heat map of snRNA-seq data with the top 20 differentially expressed genes for SST and PVALB subclass with SST FRZB highlighted in blue. Genes in subpanel are key genes for the major subclasses and classes. (B) Transcriptomic UMAP highlighting the PVALB and SST subclasses and SST FRZB in blue. (C) UMAP representation of electrophysiology space highlighting SST and PVALB subclasses and SST FRZB in blue. (D) Overlaid single action potential sweeps from SST FRZB and PVALB subclass; black lines represent the mean and are overlaid to the right for direct comparison. (E) UMAP representation of electrophysiology space color-coded by upstroke/downstroke ratio and action potential width. Box plots to the right show the distribution of data of the SST and PVALB subclasses with SST FRZB highlighted in blue. (Kruskal-Wallis

ANOVA on ranks; $P < 0.05$, FDR corrected. Post-hoc Dunn's test; **** $P < 0.0001$, FDR corrected). (F) UMAP representation of morphology space with highlighting SST and PVALB subclasses and SST FRZB in blue. (G) Morphology feature box plots for SST, SST FRZB, and PVALB. EMD, earth movers distance (Kruskal-Wallis ANOVA on ranks; $P < 0.05$, FDR corrected. Post-hoc Dunn's test; ** $P < 0.01$, FDR corrected). (H) Morphology hierarchical coclustering of SST- and PVALB-subclass neurons where values represent the number of neurons found in each morphology type. (I) Representative morphologies from SST FRZB and PVALB subclasses shown aligned to an average cortical template with associated voltage responses to a 1 s-long current step of -90 pA and rheobase +80 pA. Morphology types from (H) are shown above each reconstruction.

coclustering on all morphologies in the SST and PVALB subclasses. Clustering revealed three morphology types (1, 4, and 5) dominated by PVALB neurons and two types (3 and 6) dominated by neurons belonging to the SST subclass. We found that neurons in the SST FRZB and SST TH transcriptomic types (a related, sparsely sampled deep-layer SST transcriptomic type that also shows gene expression similarities to PVALB) more often clustered with PVALB morphology types (Fig. 3H). Juxtaposing morphologies of SST FRZB and PVALB neurons also revealed their similarity to each other, including multipolar dendrites and a dense, local axon that avoids L1 (Fig. 3I). Based on these collective, multimodal results, we suggest that SST FRZB could be considered as part of the PVALB subclass rather than SST subclass, despite higher expression of SST than PVALB for most neurons of this type. This assignment has been applied for subclass-level analyses and suggests that collecting multimodal data is critical to validate transcriptomic types, particularly for cells with not immediately clear or intermediate gene expression signatures.

Morphological heterogeneity within SST CALB1

We identified dramatic morphological heterogeneity within the main supragranular SST transcriptomic type, L1-3 SST CALB1 (hereafter called SST CALB1). In mice, Sst subclass neurons in L2/3 have classic MC shape, which is defined as having extensive L1 axon (49). In humans, we qualitatively identified four morphological types within SST CALB1. Three of these types resembled previously described neurons: MCs, DBCs, and basket-like cells (BCs). We found classic MCs at the L2-L3 border and in L3. The MCs had considerable ascending axon resulting in an extensive plexus in L1 with comparatively minimal descending axon. DBCs had a characteristic ratio of axon to dendrite width, which distinguishes these from other SST subclass neurons. We also found one SST CALB1 neuron with basket-like properties, including radially arrayed dendrite and axonal branches and minimal L1 axon innervation. The fourth morphological type, a subset of the MCs, had unusually sparse axon compared with MCs, and thus we refer to them as “sparse SST” to distinguish them from classic MCs (Fig. 4, A and B). Sparse SST neurons had somas restricted to L2, contained axons in L1, and had considerable descending axons with one instance of the axon reaching deep L5 to upper L6. Unlike other morphology types within SST CALB1, this type had a wide dendrite, long axonal extent, and sparsely branching axon that plateaued in L1 and L2 (see histograms in Fig. 4A). Our dataset contained additional SST CALB1 neurons (fig. S4) that we did not categorize into these four morphology types because of insufficient axonal information to make a confident morphological qualification.

Next, we investigated how passive and active electrophysiological properties varied for the four morphological types of SST CALB1. Despite the limited number of neurons, we observed potential trends emerging that suggest that particular features may correspond with distinct morphologically defined SST CALB1 neurons. For example, sparse SST neurons show a lower degree of sag, a higher adaptation ratio, and a slightly delayed onset of AP firing as compared with DBCs and MCs, whereas the peak of the AP is highest in MCs (Fig. 4C). These data suggest that a correspondence might exist between functional features and morphology for neurons within the heterogeneous SST CALB1 transcriptomic type. However, validation in a larger number of neurons is needed to confirm these findings.

We next sought to identify differentially expressed genes associated with the morphological heterogeneity within the SST CALB1 transcriptomic type and determine whether neurons could independently be grouped into morphological types based on gene expression. With this variable gene set, three distinct clusters appeared with morphological types largely separated across clusters (Fig. 4D). These results suggest that there are genetic correlates of distinct phenotypic properties within the SST CALB1 type.

Double bouquet cells

Among the SST CALB1 neurons, we identified the double bouquet cell type, specialized in primates (50, 51) but also discovered in other specific carnivores (52–54). DBCs are described as having a “horse-tail” morphology with ascending and descending narrow axon bundles (55). Though this morphology is well accepted in the field, the definition of molecular markers as well as their transcriptomic-type identities remain incompletely resolved (56). We found that these classical DBC morphologies map to two closely related transcriptomic types, SST CALB1, mentioned above, and L3-5 SST ADGRG6 (hereafter called SST ADGRG6). DBCs from both transcriptomic types had classic horse-tail axon collaterals extending down to L5 and frequently up to L1. They often contained multiple descending axon bundles with short perpendicular branches. In addition to a narrow axon signature, we found their dendrites to be narrow and either bitufted or multipolar (Fig. 5A). MERFISH analysis to map the spatial distributions of all types in the MTG taxonomy revealed that the SST CALB1 transcriptomic type was mostly restricted to L2, whereas SST ADGRG6 was mostly restricted to L3 (Fig. 5B), in close alignment with soma distributions from Patch-seq experiments. In agreement with the differing soma distribution patterns, we found a slight shift in their axon peak distribution, with SST CALB1 axon shifted more superficially than that of SST

ADGRG6 (Fig. 5A, histograms at right). We also found that six out of seven DBCs in the SST CALB1 transcriptomic type were from the temporal cortex, whereas three out of four DBCs in the SST ADGRG6 transcriptomic type were from the frontal cortex, suggesting a possible differential abundance or enrichment across the cortex (fig. S7A).

Given that we found DBCs within two transcriptomic types and taking into account a recent report of variable or inconsistent gene-expression signatures for morphologically defined human DBCs (56), we next sought to explore how these results compared to marker-gene expression for human DBCs in our dataset. Most DBCs showed strong expression of CALB1 (calbindin), whereas only one showed expression of CALB2 (calretinin). All but one neuron showed some degree of SST expression and mixed expression of TAC1, NOS1, and NPY (fig. S7A). With this variable expression and limited sample size, we could not identify key genes specific to morphologically defined DBCs.

To examine the functional properties of DBCs, we examined the voltage responses to hyperpolarizing and depolarizing current. DBCs displayed a range of firing patterns from accommodating and stuttering to irregular spiking (Fig. 5C). Furthermore, in the electrophysiological UMAP space, DBCs from the SST CALB1 and SST ADGRG6 transcriptomic types were intermingled with other SST neurons (Fig. 5D, middle). Representative electrophysiological features showed varying responses across individual DBCs and the two transcriptomic types. One main feature that was consistent and prominent with all DBCs was a higher sag ratio (Figs. 4C and 5C), in close agreement with the recently reported electrophysiological signature of human DBCs (56).

In morphological UMAP space, we saw DBCs from these two transcriptomic types cluster near each other with perhaps some separation at the transcriptomic-type level (Fig. 5D, right). Bouton density measurements did not show differences between the two types (Fig. 5E and fig. S7B). Therefore, we observed two distinct populations of human DBCs that were phenotypically virtually indistinguishable but had different areal enrichment and mapped to specific SST transcriptomic types occupying distinct laminar positions in the cortical depth.

Human versus mouse

Species divergence in cortical GABAergic neuronal properties could underlie putative species-specific cognitive abilities and may have important implications for translational research. For example, prior work has consistently identified higher hyperpolarization-activated cyclic nucleotide-gated (HCN)-channel expression and function in human versus mouse cortical neuron types (57, 58), which is of potential clinical relevance given that antiepileptic

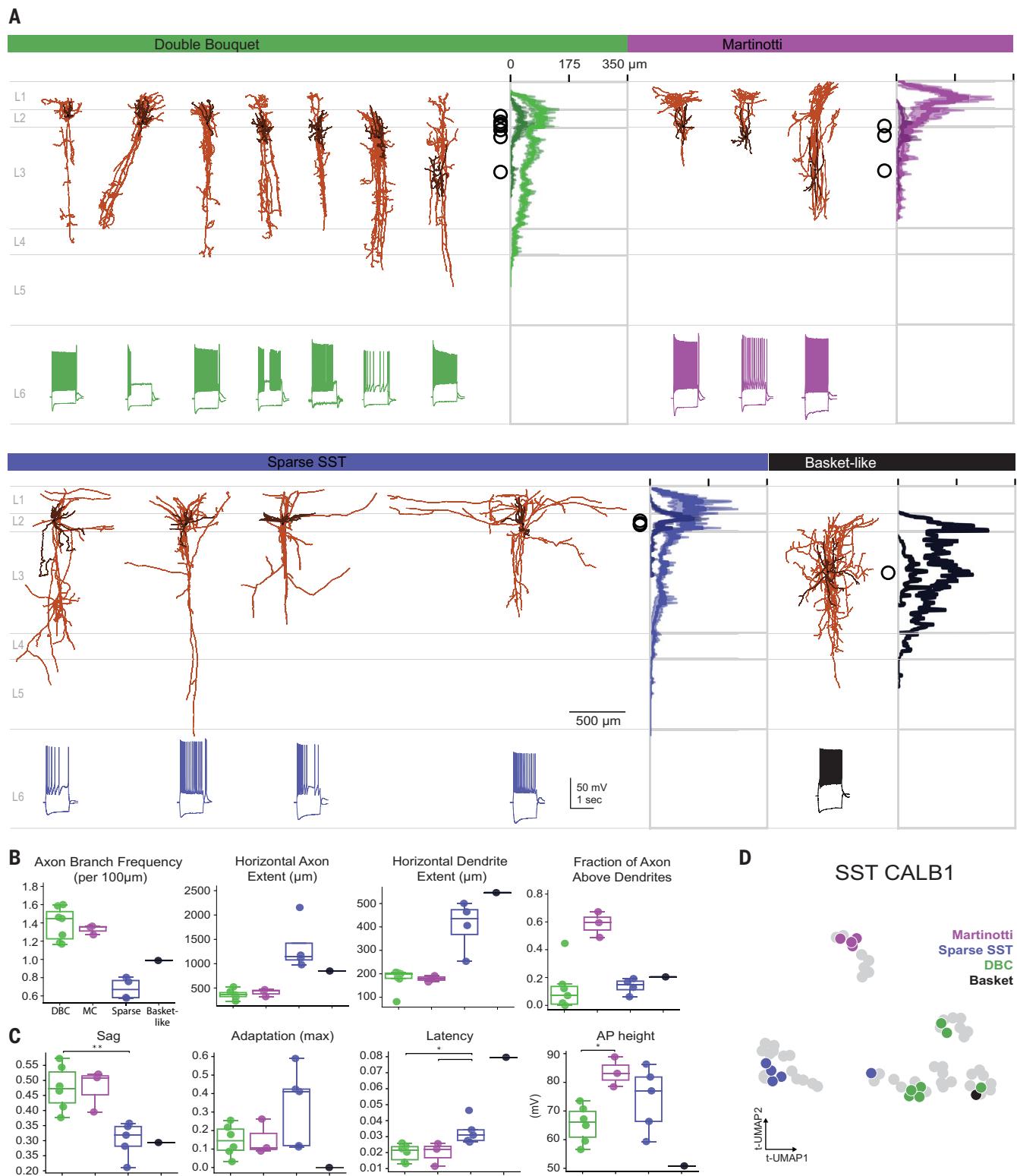


Fig. 4. Morphological heterogeneity within SST CALB1 transcriptomic type.

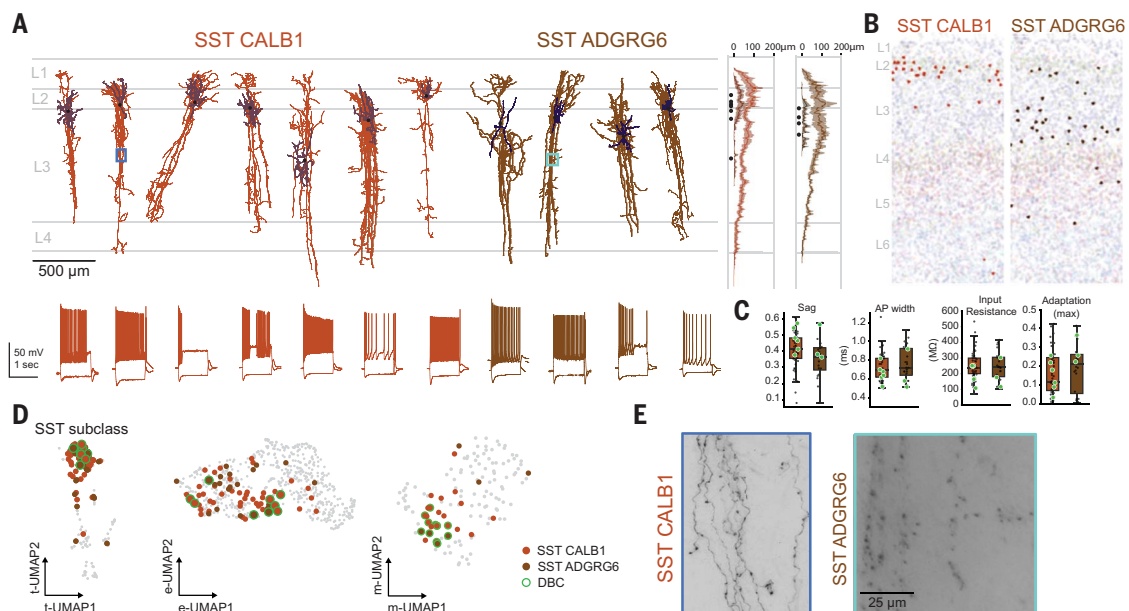
(A) Morphologies from SST CALB1 t-type categorized by qualitative morphology type shown aligned to an average cortical template, with histograms to the right of the morphologies displaying average dendrite (darker color) and axon (lighter color) branch length by cortical depth (shading shows ± 1 SD about mean; soma locations are represented by black circles). Voltage responses to a 1 s-long current step to a -90 pA and rheobase $+80$ pA are shown below. Box

plots representing key morphological (B) and electrophysiological (C) features by morphology type (Kruskal-Wallis ANOVA on ranks; $P < 0.05$, FDR corrected. Post-hoc Dunn's test; * $P < 0.05$, ** $P < 0.01$, FDR corrected). (D) UMAP of all SST CALB1 neurons based on 253 genes differentially expressed between 10 DBC, MC, and sparse SST neurons. Neurons cluster into three main groups corresponding to morphology types (colored markers). Neurons with unknown morphologies are represented by gray markers.

Fig. 5. Transcriptomic-type identity, spatial distribution, and multimodal properties of human DBCs.

(A) Putative DBC morphologies mapped to transcriptomic type SST CALB1 or SST ADGRG6 and shown aligned to an average cortical template. Histograms to the right of the morphologies display average dendrite (darker color) and axon (lighter color) branch length by cortical depth (shading shows ± 1 SD about mean; soma locations represented by black circles). (Bottom) Accompanying each reconstruction is the voltage response to a

1 s-long current step to a -90 pA and rheobase $+80$ pA for each respective DBC. (B) Spatial distribution for SST CALB1 and SST ADGRG6 revealed by MERFISH. (C) Four specific electrophysiology features shown as box or scatter plots for the SST CALB1 and SST ADGRG6 t-types with putative DBCs highlighted in green. (D) UMAP representation of transcriptomics (isolated to the SST subclass), electrophysiology, and morphology. SST CALB1 and SST ADGRG6 t-types are colored orange and brown, respectively, and qualitatively defined putative DBCs are highlighted in green. (E) 63 \times MIP inset corresponding to Fig. 4A showing axon horse-tail bundles and boutons.



drugs such as lamotrigine have been shown to activate HCN channels in dendrites (59). To directly explore the degree of conservation of cortical GABAergic subclasses from mice to humans, we compared our data with a previously published and comprehensive Patch-seq dataset of cortical GABAergic neurons in the mouse primary visual cortex (16). In previous work (1), transcriptomic types in humans and mice were aligned based on shared gene expression covariation to generate a set of genes to define mouse and human homologous cell types. We focused on supragranular neurons of two homologous types: (i) Pvalb 2, which consisted of human transcriptomic types PVALB WFDC2 and L4-6 PVALB SULF1 and mouse transcriptomic types Pvalb Calb1 Sst, Pvalb Reln Itm2a, Pvalb Reln Tac1, and Pvalb Sema3e Kank4, and (ii) Sst 5, which consisted of human SST CALB1 and mouse Sst Calb2 Necab1, Sst Calb2 Pdlim5, Sst Mme Fam114a1, Sst Tac1 Htr1d, and Sst Tac1 Tacr3.

Both Pvalb 2 and Sst 5 exhibited variations in morphological features across species (Fig. 6B). Human neurons had less axonal and dendritic branching yet occupied a larger spatial extent. We found no variation in axon total length between the homologous types. Taken together, these findings indicate that mouse neurons have a denser axonal plexus in closer proximity to their soma. In the specific case of Sst 5, several of the morphology features that differ across species reflect the change from L2/3 Martinotti neurons in mice to a more diverse set of L2 and L3 human SST morphologies that have drastically different axonal shape compared to mouse.

A variety of single-neuron electrophysiological features were found to be distinct between mice and humans. In the electrophysiological UMAP, both Pvalb 2 and Sst 5 showed clear separation between humans and mice (Fig. 6C). Average traces from each type and species shown in Fig. 6D and quantified in Fig. 6E highlight the differences in sag, rheobase, and AP half-width. Features related to AP firing such as average firing rate and AP frequency-current curve slope were found to differ across species for the Pvalb 2 but not for the Sst 5 homologous type (Fig. 6D and fig. S8B). Given that we previously established that select electrophysiological features (i.e., sag and AP width) of PVALB WFDC2 were different between the acute and culture paradigms, and given that all mouse data in this analysis was derived exclusively from acute brain slices, we sought to evaluate to what extent the slice preparation method could explain any observed species differences within Pvalb 2 or Sst 5 homologous types. Only the species difference in AP width for Pvalb 2 was driven primarily by the culture condition, whereas all other species differences in electrophysiological features were robustly detected irrespective of acute versus culture paradigm (fig. S9).

Discussion

The diversity of cortical interneurons has posed a major challenge to classify and characterize their defining properties. Our work leveraged a human MTG cell type taxonomy (1) as a reference to map the transcriptomic identities of patch clamp-recorded human cortical

GABAergic neurons in ex vivo brain slices. This taxonomy contains 45 GABAergic neuronal transcriptomic types across four canonical interneuron subclasses (PVALB, SST, VIP, and LAMP5/PAX6). In the present study, we combined viral genetic labeling with Patch-seq to target human cortical GABAergic neurons. We performed Patch-seq experiments on 778 human cortical GABAergic neurons and aggregated our data at the subclass level to uncover the signature morphoelectric properties of these canonical human interneuron subclasses, and where feasible, dove deeper into features of select GABAergic transcriptomic types. Although many of the GABAergic transcriptomic types were not sampled at sufficient depth to conclude their defining properties in this study, our dataset achieved coverage of 44 of the 45 GABAergic transcriptomic types, many of which represent rare cell types.

We characterized the changes that occurred in this short-term slice culture and viral-labeling paradigm in multiple data modalities including gene expression and electrophysiological and morphological features (where sampling depth permitted). Although discrete changes were evident and described in electrophysiology, these putative culture differences did not preclude or hinder high confidence mapping of recorded neurons to GABAergic subclasses and transcriptomic types in the human MTG taxonomy. This is well explained by the fact that marker genes important for mapping at the GABAergic subclass level were robustly detected overall and minimally impacted by slice culture or viral transduction. Additionally,

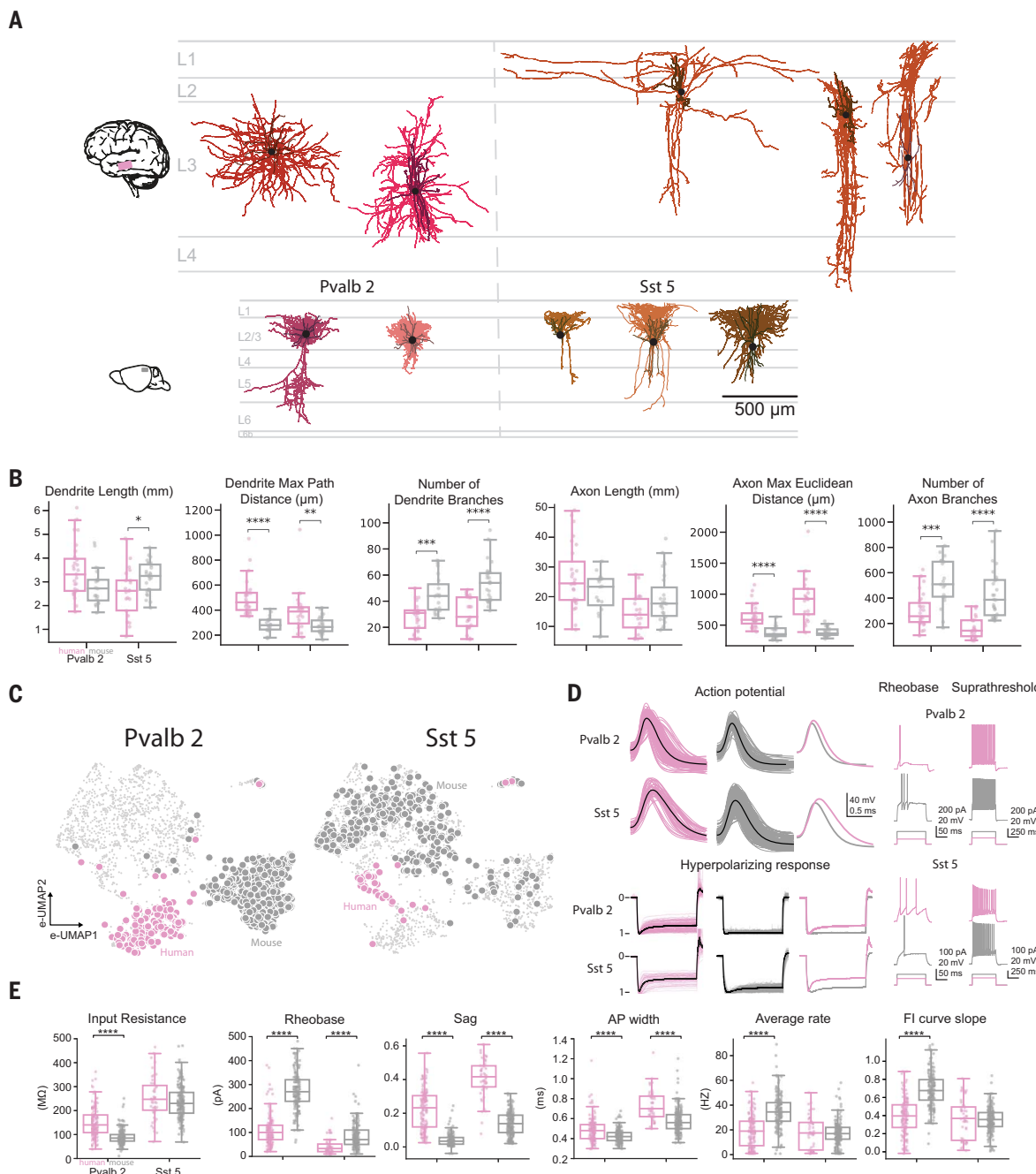


Fig. 6. Species differences in morphoelectric properties for homologous types Pvalb 2 and Sst 5. (A) Human and mouse representative morphologies, aligned to average cortical templates, from homologous types Pvalb 2 and Sst 5 with each t-type represented by different colors. (B) Box plots of select morphological features from humans (pink) and mice (gray) (FDR-corrected Mann-Whitney test; *P < 0.05, **P < 0.01, ***P < 0.001, ****P < 0.0001). (C) Electrophysiology UMAP for mouse and human SST/PVALB neurons. (Left) Homologous type Pvalb 2 and (Right) homologous type Sst 5 with pink markers representing human and gray representing mouse. (D) Overlaid single action potential sweeps

from human and mouse homologous types Pvalb 2 and Sst 5. Black lines represent the mean and are overlaid to the right for direct comparison. Overlaid and normalized voltage response to a 1-s –90 pA hyperpolarizing current step. Black lines represent the mean of the group and are overlaid to the right for direct comparison. Voltage responses to depolarizing current at rheobase and rheobase +110 pA from human and mouse homologous types Pvalb 2 and Sst 5. (E) Box plots of select distinguishing electrophysiological features from homologous types Pvalb 2 and Sst 5 in mice and humans. Asterisks indicate significant pairwise comparisons; ****P < 0.0001, FDR-corrected Mann-Whitney test.

upon further analysis of voltage-gated ion-channel genes, expression of 7 out of 114 genes was different between the two paradigms. Three of the seven were genes that code for sodium channel subunits, which may explain some of

the differences we observed in select features such as AP width. We identified a gene expression signature in a subset of our dataset that corresponded to a module of microglia-related genes. This identical signature was

observed for both neurons recorded in acute and cultured slices (but is more pronounced in culture) and has been similarly observed in other human and mouse acute brain slice Patch-seq datasets (15–17, 36, 37). Further work is

warranted to understand the cause and consequences of this gene expression signature in brain slice experiments.

Viral genetic targeting with Patch-seq experiments enhanced the coverage of transcriptomic types in the SST subclass and allowed us to aggregate a sizable dataset of neurons that map to SST CALB1. These neurons exhibited high heterogeneity in morphoelectric features that might seem incongruent with the mapping outcome to a single transcriptomic type in the taxonomy. At least three discrete morphological types were recognized including DBCs with classical descending long horse-tail axon bundles (55), MCs with ascending axons reaching L1, and a type we labeled sparse SST for the sparsely branched and lengthy axon segments. Further grouping by morphology type within this SST CALB1 transcriptomic type revealed strong coherence of electrophysiological features with many distinctive features between groups. These results suggest that further splitting of the SST CALB1 transcriptomic type may be warranted but will require additional studies to fully resolve, presumably requiring deeper multimodal phenotypic characterization.

Another important outcome from our study is the delineation of the transcriptomic types containing human DBCs. In addition to SST CALB1 transcriptomic-type mapping, we also observed DBCs mapping to a second transcriptomic type in the SST subclass, SST ADGRG6. DBCs mapping to SST CALB1 were predominantly found in the temporal cortex, whereas DBCs mapping to SST ADGRG6 were enriched in the frontal cortex, which suggests possible regional differences in abundance of these putative DBC subtypes across the human cortex. Furthermore, spatial transcriptomics revealed a clear shift in laminar distribution between the two transcriptomic types, with SST CALB1 soma distribution mostly restricted to L2, and SST ADGRG6 soma distribution mostly restricted to L3. DBCs sampled from Patch-seq experiments follow this trend of distinct laminar positioning of the two transcriptomic types. We were not able to discriminate DBCs versus non-DBC within these transcriptomic types using current available spatial methodologies. Nonetheless, these data are consistent with the existence of at least two subtypes of human DBCs. Whether these transcriptomically defined subtypes align to previously reported DBC subtypes in the human cortex (54) or if there exist functional specializations between these subtypes remains to be determined. Our findings corroborate and extend recent work (56) and provide important clues about the molecular identity, synaptic connectivity, and function of human DBCs. The overall picture from these two independent studies is that human DBCs are more heterogeneous than previously understood.

A limitation of the current dataset was the low number of neurons with classic Martinotti morphologies in the SST subclass. This may be the result of biased sampling of supragranular layers in our experiments, whereas MCs could instead be more abundant in infragranular layers of the human neocortex. The abundance and spatial distribution of MCs in the human cortex has not been detailed to our knowledge. We observed denser GABAergic neuron labeling in L2 and L3 with the CN1390 GABAergic enhancer AAV vector, which suggests possible enrichment for GABAergic neuron types most abundant in these layers (i.e., SST CALB1). However, other neuron types with expected enrichment in supragranular layers such as chandelier cells and many diverse transcriptomic types of the VIP subclass were poorly sampled in this study. The underlying explanation remains unclear, but one possibility may be laminar shifts in these cell types in the human versus rodent cortex in light of prior findings of laminar shifts, or variation by cortical area in cell-type marker genes in the mouse versus human neocortex (60). Changes in the abundance or laminar distribution of cell types can be resolved with spatial transcriptomics approaches applied in mouse versus human brain samples or by comparing across diverse mammalian species (1, 18). For example, chandelier cells are known to be enriched at the L1-L2 border in the mouse cortex (61) but instead show enrichment at the L3-L4 border in the human temporal cortex (1). Rapid progress in single-cell epigenetic data generation (62–65) and continued discovery of brain cell type-specific enhancers suitable for use in viral vectors (35, 66–68) are likely to be the key to targeted analysis of these and other important human cortical interneuron types. Indeed, we have demonstrated proof of concept for improved sampling of VIP subclass neurons in human neocortical slices using an enhancer AAV vector. Because of the wide diversity of transcriptomic types in the VIP subclass and the limited sampling achieved in our dataset by using the more general GABAergic labeling approach, viral tools such as this are likely to hasten the progress for deeper multimodal analysis of poorly sampled human VIP transcriptomic types.

Perhaps the most impactful finding of our study is the direct demonstration of how multimodal Patch-seq data are vital to refinement of transcriptomic cell type taxonomies. Based only on transcriptomics, no clear assignment of SST FRZB to SST or PVALB subclass was possible, and this inherent ambiguity is likely rooted in the shared developmental origin of SST and PVALB subclasses (46). However, our electrophysiology and morphology results clearly resolve that the phenotypic properties of SST FRZB transcriptomic type are most parsimonious with PVALB subclass assignment

in the human neocortical cell type taxonomy. This underscores the notion that cellular taxonomies built on single-cell transcriptomes and differential gene expression are not static, but rather represent a starting foundation to build upon as new data modalities are obtained and aligned at the resolution of transcriptomic types. Thus, transcriptomic cell type taxonomies are necessary but not always sufficient to infer meaningful functional types with high accuracy. Alignment of multimodal data such as spatial distribution and abundance, cellular morphology, axonal projections and connectivity, neuromodulation, and intrinsic and synaptic electrophysiological properties will be essential to refine and extend foundational cellular taxonomies of the brain.

In this study, we have provided a first-order characterization of the signature morphoelectric properties of the canonical human cortical GABAergic neuron subclasses and select transcriptomic types. Despite the apparent conservation of canonical cortical GABAergic subclasses, we uncovered previously unrecognized species differences in fundamental morphological and electrophysiological features of neocortical PVALB and SST homologous types. Precisely how such anatomical and functional differences contribute to specific human cognitive abilities or to selective vulnerability of discrete neuron types in disease remains to be determined. This work provides a promising roadmap for future functional studies of human brain cell types at the resolution of emerging transcriptomic cell type taxonomies and provides a rich open-access dataset for exploring gene-function relationships for a wide diversity of human neocortical GABAergic neuron types.

Materials and Methods

Human tissue acquisition

Surgical specimens were obtained from local hospitals (Harborview Medical Center, Swedish Medical Center, and University of Washington Medical Center) in collaboration with local neurosurgeons. Data included in this study were obtained from neurosurgical tissue resections for the treatment of refractory temporal lobe epilepsy or deep brain tumor. All patients provided informed consent and experimental procedures were approved by hospital institute review boards before commencing the study. Tissue was placed in slicing artificial cerebral spinal fluid (ACSF) as soon as possible following resection. Slicing ACSF comprised (in mM): 92 N-methyl-D-glucamine chloride (NMDG-Cl), 2.5 KCl, 1.2 Na₂PO₄, 30 NaHCO₃, 20 4-(2-hydroxyethyl)-1-piperazineethanesulfonic acid (HEPES), 25 D-glucose, 2 thiourea, 5 sodium-L-ascorbate, 3 sodium pyruvate, 0.5 CaCl₂·4H₂O, and 10 MgSO₄·7H₂O. Before use, the solution was equilibrated with 95% O₂, 5% CO₂ and the pH was adjusted to 7.3 by addition of 5N HCl solution. Osmolality was verified to be between

295 to 305 mOsm kg⁻¹. Human surgical tissue specimens were immediately transported (15 to 35 min) from the hospital site to the laboratory for further processing.

Human neurosurgical specimens and ethical compliance

The neurosurgical tissue specimens collected for this study were apparently non-pathological tissues removed during the normal course of surgery to access underlying pathological tissues. Tissue specimens were determined to be nonessential for diagnostic purposes by medical staff and would have otherwise been discarded. Tissue procurement from neurosurgical donors was performed outside of the supervision of the Allen Institute at a local hospital and tissue was provided to the Allen Institute under the authority of the institutional review board of the participating hospital. A hospital-appointed case coordinator obtained informed consent from the donor before surgery. Tissue specimens were deidentified before receipt by Allen Institute personnel.

Tissue processing

Human acute and cultured brain slices (350 µm) were prepared with a Compresstome VF-300 (Precisionary Instruments) modified for block-face image acquisition (Mako G125B PoE camera with custom integrated software) before each section to aid in registration to the common reference atlas. Brains or tissue blocks were mounted to preserve intact pyramidal neuron apical dendrites within the brain slice. Slices were transferred to a carbogenated (95% O₂/5% CO₂) and warmed (34°C) slicing ACSF to recover for 10 min according to the NMDG protective recovery method (69). Acute brain slices were then transferred to room temperature holding ACSF of the composition (in mM): 92 NaCl, 2.5 KCl, 1.2 NaH₂PO₄, 30 NaHCO₃, 20 HEPES, 25 D-glucose, 2 thiourea, 5 sodium-L-ascorbate, 3 sodium pyruvate, 2 CaCl₂·4H₂O and 2 MgSO₄·7H₂O for the remainder of the day until transferred for patch clamp recordings. Before use, the solution was equilibrated with 95% O₂, 5% CO₂ and the pH was adjusted to 7.3 using NaOH. Osmolality was verified to be between 295 to 305 mOsm kg⁻¹. Alternately, slices for interface culture were placed onto membrane inserts (Millipore) in 6 well plates with 1 mL per well of slice culture media of the composition: 8.4 g/L MEM Eagle medium, 20% heat-inactivated horse serum, 30 mM HEPES, 13 mM d-glucose, 15 mM NaHCO₃, 1 mM ascorbic acid, 2 mM MgSO₄·7H₂O, 1 mM CaCl₂·4H₂O, 0.5 mM GlutaMAX-I and 1 mg/L insulin. The slice culture medium was carefully adjusted to pH 7.2 to 7.3 and osmolality of 300 to 310 mOsmoles per kilogram by addition of pure H₂O, sterile-filtered and stored at 4°C for up to 2 weeks. Culture plates were placed in a humidified 5% CO₂ incubator at 35°C, and the

slice culture medium was replaced every two to three days until endpoint analysis. One to three hours after brain slices were plated on cell culture inserts, brain slices were infected by direct application of concentrated AAV viral particles over the slice surface (34).

AAV vector cloning and viral packaging

The DLX2.0 enhancer consists of 3 concatenated copies of the DLX core enhancer region (70). The ultraconserved 131 bp core DLX enhancer region has 100% linear sequence identity between mouse and human. The DLX2.0 fragment was custom gene synthesized and subcloned by standard restriction enzyme digestion and ligation into a recombinant AAV vector backbone upstream of the beta globin minimal promoter, SYFP2 reporter transgene, short woodchuck hepatitis virus posttranscriptional regulatory element (WPRE3) and bovine growth hormone (BGH) polyA sequence to produce AAV vector CN1390. The CN1390 plasmid map as well as plasmid DNA and PHP.eB serotype viral aliquots are available from Addgene (plasmid #163505). The VIP enhancer candidate eHGTC_354h was selected using previously published human single cell ATAC-seq data (35) based on proximity to the surrogate VIP subclass marker gene CALB2 and accessible ATAC-seq peak exclusively in the VIP subclass versus all other cortical cell type subclasses in the dataset. The candidate genomic enhancer was PCR amplified from human genomic DNA and cloned by standard restriction enzyme digestion and ligation into a recombinant AAV vector backbone as mentioned above (but containing a custom designed 3XSP10 insulator sequence 5'-gaaggtagccctaaacacactattctacacacagaaaaatgtttcacttaggaagctaccctaaacacactattctacacacagaaaaatgtttcacttaggaagctaccctaaacacactattctacacacagaaaaatgtttcacttag-3' upstream of the enhancer position) to yield AAV vector CN2039. The CN2039 plasmid map as well as plasmid DNA will be available from Addgene (plasmid #208401).

Enhancer AAV plasmids CN1390 and CN2039 were maxi-prepped and transfected with PEI Max 40K (Polysciences Inc., catalog # 24765-1) into one 15-cm plate of AAV-293 cells (Cell Biolabs catalog # AAV-100), along with helper plasmid pHelper (Cell BioLabs) and PHP.eB rep/cap packaging plasmid (Chan *et al.*, 2017), with a total mass of 150 µg PEI Max 40K, 30 µg pHelper, 15 µg rep/cap plasmid, and 15 µg enhancer-AAV vector. The next day medium was changed to 1% FBS, and then after 5 days, cells and supernatant were harvested and AAV particles released by three freeze-thaw cycles. Lysate was treated with benzonase after freeze thaw to degrade free DNA (2 µL benzonase, 30 min at 37 degrees, MilliporeSigma catalog # E8263-25KU), and then cell debris was precleared with low-speed spin (1500 g 10 min), and finally the crude virus was concentrated over a 100 kDa molecular weight cutoff Centricon

column (MilliporeSigma catalog # Z648043) to a final volume of ~150 µL. For highly purified large-scale preps this protocol was altered so that ten plates were transfected and harvested together at 3 days after transfection, and then the crude virus was purified by iodixanol gradient centrifugation.

Patch clamp recording

Slices were continuously perfused (2 mL/min) with fresh, warm (34°C) recording ACSF containing the following (in mM): 126 NaCl, 2.5 KCl, 1.25 Na₂PO₄, 26 NaHCO₃, 12.5 D-glucose, 2 CaCl₂·4H₂O and 2 MgSO₄·7H₂O (pH 7.3) and continuously bubbled with 95% O₂/5% CO₂. The bath solution contained blockers of fast glutamatergic (1 mM kynurenic acid) and GABAergic synaptic transmission (0.1 mM picrotoxin). Thick-walled borosilicate glass (Warner Instruments, G150F-3) electrodes were manufactured (Narishige PC-10) with a resistance of 4–5 MΩ. Before recording, the electrodes were filled with ~1.0 to 1.5 μL of internal solution with biocytin [110 mM potassium gluconate, 10.0 mM HEPES, 0.2 mM ethylene glycol-bis (2-aminoethyl ether)-N,N,N',N'-tetraacetic acid, 4 mM potassium chloride, 0.3 mM guanosine 5'-triphosphate sodium salt hydrate, 10 mM phosphocreatine disodium salt hydrate, 1 mM adenosine 5'-triphosphate magnesium salt, 20 μg/mL glycogen, 0.5 U/μL RNase inhibitor (Takara, 2313A) and 0.5% biocytin (Sigma B4261), pH 7.3]. The pipette was mounted on a Multiclamp 700B amplifier headstage (Molecular Devices) fixed to a micromanipulator (PatchStar, Scientifica).

The composition of bath and internal solution as well as preparation methods were chosen to maximize the tissue quality of slices from adult mice, to align with solution compositions typically used in the field (to maximize the chance of comparison to previous studies), modified to reduce RNase activity and ensure maximal gain of mRNA content.

Electrophysiology signals were recorded using an ITC-18 Data Acquisition Interface (HEKA). Commands were generated, signals processed, and amplifier metadata were acquired using MIES written in Igor Pro (WaveMetrics). Data were filtered (Bessel) at 10 kHz and digitized at 50 kHz. Data were reported uncorrected for the measured (Neher, 1992)-14 mV liquid junction potential between the electrode and bath solutions.

Prior to data collection, all surfaces, equipment, and materials were thoroughly cleaned in the following manner: a wipe down with DNA away (Thermo Scientific), RNase Zap (Sigma-Aldrich), and finally nuclease-free water. After formation of a stable seal and break-in, the resting membrane potential of the neuron was recorded (typically within the first minute). A bias current was injected, either manually or automatically using algorithms within the MIES data acquisition package, for the remainder of

the experiment to maintain that initial resting membrane potential. Bias currents remained stable for a minimum of 1 s before each stimulus current injection.

To be included in analysis, a neuron needed to have a $>1\text{ G}\Omega$ seal recorded before break-in and an initial access resistance $<20\text{ M}\Omega$ and $<15\%$ of the Rinput. To stay below this access resistance cut-off, neurons with a low input resistance were successfully targeted with larger electrodes. For an individual sweep to be included, the following criteria were applied: (i) the bridge balance was $<20\text{ M}\Omega$ and $<15\%$ of the Rinput; (ii) bias (leak) current $0 \pm 100\text{ pA}$; and (iii) root mean square noise measurements in a short window (1.5 ms, to gauge high frequency noise) and longer window (500 ms, to measure patch instability) were <0.07 and 0.5 mV , respectively.

Upon completion of electrophysiological examination, the pipette was centered on the soma or placed near the nucleus (if visible). A small amount of negative pressure was applied ($\sim 30\text{ mbar}$) to begin cytosol extraction and attract the nucleus to the tip of the pipette. After approximately one minute, the soma had visibly shrunk and/or the nucleus was near the tip of the pipette. While maintaining the negative pressure, the pipette was slowly retracted in the x and z direction. Slow, continuous movement was maintained while monitoring pipette seal. Once the pipette seal reached $>1\text{ G}\Omega$ and the nucleus was visible on the tip of the pipette, the speed was increased to remove the pipette from the slice. The pipette containing internal solution, cytosol, and nucleus was removed from the pipette holder and contents were expelled into a PCR tube containing lysis buffer (Takara, 634894).

Transcriptomic Data Collection

cDNA amplification and library construction

We used the SMART-Seq v4 Ultra Low Input RNA Kit for Sequencing (Takara, 634894) to reverse transcribe poly(A) RNA and amplify full-length cDNA according to the manufacturer's instructions. We performed reverse transcription and cDNA amplification for 20 PCR cycles in 0.65 ml tubes, in sets of 88 tubes at a time. At least one control eight-strip was used per amplification set, which contained four wells without cells and four wells with 10 pg control RNA. Control RNA was either Universal Human RNA (UHR) (Takara 636538) or control RNA provided in the SMART-Seq v4 kit. All samples proceeded through Nextera XTDNA Library Preparation (Illumina FC-131-1096) using either Nextera XT Index Kit V2 Sets A-D (FC-131-2001, 2002, 2003, 2004) or custom dual-indexes provided by IDT (Integrated DNA Technologies). Nextera XT DNA Library prep was performed according to manufacturer's instructions, except that the volumes of all reagents including cDNA input

were decreased to $0.2 \times$ by volume. Each sample was sequenced to approximately 500 k reads.

RNA-sequencing

Fifty-base-pair paired-end reads were aligned to GRCh38 (mm10) using a RefSeq annotation gff file retrieved from NCBI on 18 January 2016 (https://www.ncbi.nlm.nih.gov/genome/annotation_euk/ all). Sequence alignment was performed using STAR v2.5.3 (71) in two pass Mode. PCR duplicates were masked and removed using STAR option "bamRemoveDuplicates". Only uniquely aligned reads were used for gene quantification. Gene counts were computed using the R Genomic Alignments package (72). Overlaps function using "IntersectionNotEmpty" mode for exonic and intronic regions separately. Exonic and intronic reads were added together to calculate total gene counts; this was done for both the reference dissociated cell data set and the Patch-seq data set of this study.

SMART-seq v4 RNA-sequencing

The SMART-Seq v4 Ultra Low Input RNA Kit for Sequencing (Takara #634894) was used per the manufacturer's instructions. Standard controls were processed with each batch of experimental samples as previously described. After reverse transcription, cDNA was amplified with 21 PCR cycles. The NexteraXT DNA Library Preparation (Illumina FC-131-1096) kit with NexteraXT Index Kit V2 Sets A-D (FC-131-2001, 2002, 2003, or 2004) was used for sequencing library preparation. Libraries were sequenced on an Illumina HiSeq 2500 instrument (Illumina HiSeq 2500 System, RRID: SCR_016383) using Illumina High Output V4 chemistry. The following instrumentation software was used during data generation workflow; SoftMax Pro v6.5; VWorks v11.3.0.1195 and v13.1.0.1366; Hamilton Run Time Control v4.4.0.7740; Fragment Analyzer v1.2.0.11; Mantis Control Software v3.9.7.19.

SMART-seq v4 gene expression quantification

Raw read (fastq) files were aligned to the GRCh38 human genome sequence (Genome Reference Consortium, 2011) with the RefSeq transcriptome version GRCh38.p2 (RefSeq, RRID:SCR_003496, current as of 4/13/2015) and updated by removing duplicate Entrez gene entries from the gtf reference file for STAR processing. For alignment, Illumina sequencing adapters were clipped from the reads using the fastqMCF program (from ea-utils). After clipping, the paired-end reads were mapped using Spliced Transcripts Alignment to a Reference (STAR v2.7.3a, RRID:SCR_015899) using default settings. Reads that did not map to the genome were then aligned to synthetic construct (that is ERCC) sequences and the *E. coli* genome (version ASM584v2). Quantification was performed using summarizeOverlaps from the R package GenomicAlignments v1.18.0.

Expression counts were calculated as counts per million (CPM) of exonic plus intronic reads.

Anatomical Annotations

Layer annotation and alignment

To characterize the position of biocytin-labeled cells, a $20\times$ brightfield and fluorescent image of DAPI (4',6-diamidino-2-phenylindole) stained tissue was captured and analyzed to determine layer position. Using the brightfield and DAPI image, soma position and laminar borders were manually drawn for all neurons and were used to calculate depth relative to the pia, white matter, and/or laminar boundaries. Laminar locations were calculated by finding the path connecting pia and white matter that passed through the cell's soma coordinate, and measuring distance along this path to laminar boundaries, pia and white matter.

For reconstructed neurons, laminar depths were calculated for all segments of the morphology, and these depths were used to create a "layer-aligned" morphology by first rotating the pia-to-WM axis to vertical, then projecting the laminar depth of each segment onto an average cortical layer template.

Human brain region pinning

Available surgical photodocumentation (MRI or brain model annotation) is used to place the human tissue blocks in approximate 3D space by matching the photodocumentation to a MRI reference brain volume "ICBM 2009b Nonlinear Symmetric" (73), with Human CCF overlaid (74) within the ITK-SNAP interactive software.

Morphological Reconstruction

A horseradish peroxidase (HRP) enzyme reaction using diaminobenzidine (DAB) as the chromogen was used to visualize the filled cells after electrophysiological recording, and 4,6-diamidino-2-phenylindole (DAPI) stain was used to identify cortical layers as described previously (15).

Imaging of biocytin-labeled neurons

Mounted sections were imaged as described previously (48). In brief, operators captured images on an upright AxioImager Z2 microscope (Zeiss, Germany) equipped with an Axiocam 506 monochrome camera and 0.63 \times Optivar lens. Two-dimensional tiled overview images were captured with a 20 \times objective lens (Zeiss Plan-NEOFLUAR 20 \times /0.5) in bright-field transmission and fluorescence channels. Tiled image stacks of individual cells were acquired at higher resolution in the transmission channel only for the purpose of automated and manual reconstruction. Light was transmitted using an oil-immersion condenser (1.4 NA). High-resolution stacks were captured with a 63 \times objective lens (Zeiss Plan-Apochromat 63 \times /1.4 Oil or Zeiss LD LCI Plan-Apochromat 63 \times /1.2 Imm Corr) at an interval of 0.28 μm (1.4 NA

objective) or 0.44 μm (1.2 NA objective) along the z axis. Tiled images were stitched in ZEN software and exported as single-plane TIFF files.

Morphological reconstruction

Reconstructions of the dendrites and the axon were generated for a subset of neurons with good quality transcriptomics, electrophysiology and biocytin fill. Prior to prioritizing a neuron for reconstruction, the location of the axon exiting the soma or dendrite is determined by examining the neuron in the z-depth of the 63× image stack. We then assess the direction in which the axon is heading relative to the surface of the slice. Based on this assessment, we prioritize the reconstruction of neurons whose axons remain largely within the plane of the slice. Reconstructions were generated based on a 3D image stack that was run through a Vaa3D-based image processing and reconstruction pipeline (Peng *et al.*, 2010). For some neurons images were used to generate an automated reconstruction of the neuron using TReMAP (Zhou *et al.*, 2016). Alternatively, initial reconstructions were created manually using the reconstruction software PyKNOSSOS (<https://www.ariadne.ai/>) or the citizen neuroscience game Mozak (Roskams and Popović, 2016) (<https://www.mozakscience/>). Automated or manually initiated reconstructions were then extensively manually corrected and curated using a range of tools (for example, virtual finger and polyline) in the Mozak extension (Zoran Popovic, Center for Game Science, University of Washington) of Terafly tools (75, 76) in Vaa3D. Every attempt was made to generate a completely connected neuronal structure while remaining faithful to image data. If axonal processes could not be traced back to the main structure of the neuron, they were left unconnected.

MERFISH data generation

Human postmortem frozen brain tissue was embedded in Optimum Cutting Temperature medium (VWR, 25608-930) and sectioned on a Leica cryostat at -17°C at 10 μm onto Vizgen MERSCOPE coverslips. These sections were then processed for MERSCOPE imaging according to the manufacturer's instructions. Briefly: sections were allowed to adhere to these coverslips at room temperature for 10 min prior to a 1 min wash in nuclease-free phosphate buffered saline (PBS) and fixation for 15 min in 4% paraformaldehyde in PBS. Fixation was followed by three 5 min washes in PBS prior to a 1 min wash in 70% ethanol. Fixed sections were then stored in 70% ethanol at 4°C prior to use and for up to one month. Human sections were photobleached using a 150W LED array for 72 hours at 4°C prior to hybridization then washed in 5 ml Sample Prep Wash Buffer (VIZGEN 20300001) in a 5 cm petri dish. Sections were then incubated in 5 ml Formamide

Wash Buffer (VIZGEN 20300002) at 37°C for 30 min. Sections were hybridized by placing 50 μl of VIZGEN-supplied Gene Panel Mix onto the section, covering with parafilm and incubating at 37°C for 36 to 48 hours in a humidified hybridization oven. Following hybridization, sections were washed twice in 5 ml Formamide Wash Buffer for 30 min at 47°C. Sections were then embedded in acrylamide by polymerizing VIZGEN Embedding Premix (VIZGEN 20300004) according to the manufacturer's instructions. Sections were embedded by inverting sections onto 110 μl of Embedding Premix and 10% Ammonium Persulfate (Sigma A3678) and TEMED (BioRad 161-0800) solution applied to a Gel Slick (Lonza 50640) treated 2x3 glass slide. The coverslips were pressed gently onto the acrylamide solution and allowed to polymerize for 1.5h. Following embedding, sections were cleared for 24 to 48 hours with a mixture of VIZGEN Clearing Solution (VIZGEN 20300003) and Proteinase K (New England Biolabs P8107S) according to the Manufacturer's instructions. Following clearing, sections were washed twice for 5 min in Sample Prep Wash Buffer (PN 20300001). VIZGEN DAPI and PolyT Stain (PN 20300021) was applied to each section for 15 min followed by a 10 min wash in Formamide Wash Buffer. Formamide Wash Buffer was removed and replaced with Sample Prep Wash Buffer during MERSCOPE set up. 100 μl of RNase Inhibitor (New England BioLabs M0314L) was added to 250 μl of Imaging Buffer Activator (PN 203000015) and this mixture was added through the cartridge activation port to a pre-thawed and mixed MERSCOPE Imaging cartridge (VIZGEN PN1040004). 15 ml mineral oil (Millipore-Sigma m5904-6X500ML) was added to the activation port and the MERSCOPE fluidics system was primed according to VIZGEN instructions. The flow chamber was assembled with the hybridized and cleared section coverslip according to VIZGEN specifications and the imaging session was initiated after collection of a 10X mosaic DAPI image and selection of the imaging area. For specimens that passed minimum count threshold, imaging was initiated, and processing completed according to VIZGEN proprietary protocol. Following image processing and segmentation, cells with fewer than 50 transcripts are eliminated, as well as cells with volumes falling outside a range of 100 to 300 μm.

The 140-gene Human cortical panel was selected using a combination of manual and algorithmic based strategies requiring a reference single cell/nucleus RNA-seq dataset from the same tissue, in this case the human MTG snRNAseq dataset and resulting taxonomy (1). First, an initial set of high-confidence marker genes are selected through a combination of literature search and analysis of the reference data. These genes are used as input for a greedy algorithm (detailed below). Second, the refer-

ence RNA-seq data set is filtered to only include genes compatible with mFISH. Retained genes need to be (i) long enough to allow probe design (>960 base pairs); (ii) expressed highly enough to be detected (FPKM ≥ 10), but not so high as to overcrowd the signal of other genes in a cell (FPKM < 500); (iii) expressed with low expression in off-target cells (FPKM < 50 in nonneuronal cells); and (iv) differentially expressed between cell types (top 500 remaining genes by marker score20). To more evenly sample each cell type, the reference dataset is also filtered to include a maximum of 50 cells per cluster.

The main step of gene selection uses a greedy algorithm to iteratively add genes to the initial set. To do this, each cell in the filtered reference data set is mapped to a cell type by taking the Pearson correlation of its expression counts with each cluster median using the initial gene set of size n, and the cluster corresponding to the maximum value is defined as the “mapped cluster.” The “mapping distance” is then defined as the average cluster distance between the mapped cluster and the originally assigned cluster for each cell. In this case a weighted cluster distance, defined as one minus the Pearson correlation between cluster medians calculated across all filtered genes, is used to penalize cases where cells are mapped to very different types, but an unweighted distance, defined as the fraction of cells that do not map to their assigned cluster, could also be used. This mapping step is repeated for every possible $n + 1$ gene set in the filtered reference data set, and the set with minimum cluster distance is retained as the new gene set.

These steps are repeated using the new get set (of size $n + 1$) until a gene panel of the desired size is attained. Code for reproducing this gene selection strategy is available as part of the mfishtools R library (<https://github.com/AllenInstitute/mfishtools>).

H5ad creation: Any genes not matched across both the MERSCOPE gene panel and the mapping taxonomy were filtered from the dataset before starting. From there, cluster means were calculated by dividing the number of cells per cluster by the number of clusters collected. Next, we created a training dataset by finding marker genes for each cluster by calculating the l2norm between all clusters and the mean counts of each gene per cluster. This training dataset was fed into a knn alongside the MERSCOPEs cell by gene panel to iteratively calculate best possible gene matches per cluster. All scripts and data used are available at: <https://github.com/AllenInstitute/>.

Analysis

Patch-seq data curation and mapping

To evaluate the mapping quality of Patch-seq samples, we calculated the NMS score - a ratio of “on” and “off” markers by subclass (14, 16, 40).

A value of 0.4 was designated as a cut off for low- and high-quality data. Only cells mapping to GABAergic interneuron types and that had a NMS score >0.4 were included in the analyses for this study.

Reference transcriptomic data used in this study were obtained from dissociated nuclei collected from human MTG (1), and are publicly accessible at the Allen Brain Map data portal (<https://portal.brain-map.org/atlas-and-data/rnaseq>). This taxonomy consists of a hierarchical dendrogram of cell types, along with a set of marker genes defined to distinguish types at each split in the tree. The Patch-seq transcriptomes were mapped to the reference taxonomy following the tree-mapping method (map_dend_membership in the scratch.hcat package) as described previously (36, 48). Briefly, at each branch point of the taxonomy we computed the correlation of the mapped cell's gene expression with that of the reference cells on each branch, using the markers associated with that branch point (that is, the genes that best distinguished those groups in the reference), and chose the most correlated branch. The process was repeated until reaching the leaves of the taxonomy. To determine the confidence of mapping, we applied 100 bootstrapped iterations at each branch point, and in each iteration 70% of the reference cells and 70% of markers were randomly sampled for mapping. The percentage of times a cell was mapped to a given transcriptomic type was defined as the mapping probability, and the highest probability transcriptomic type was assigned as the mapped cell type.

Electrophysiology feature analysis

For all electrophysiology stimuli that elicited spiking, APs were detected by first 40 identifying locations where the smoothed derivative of the membrane potential (dV/dt) exceeded 20 mV ms^{-1} , then refining on the basis of several criteria including threshold-to-peak voltage, time differences and absolute peak height. For each AP, threshold, height, width (at half-height), fast after-hyperpolarization (AHP) and interspike trough were calculated (trough and AHP were measured relative to threshold), along with maximal upstroke and downstroke 45 rates dV/dt and the upstroke/downstroke ratio (that is, ratio of the peak upstroke to peak downstroke). Following spike detection, summary features were calculated from sweeps with long square pulse current injection: input resistance (all hyperpolarizing sweeps, -10 to -90 pA), sag (hyperpolarizing sweep with response closest to -100 mV , generally -90 pA stimulus, and depolarizing sag on subthreshold response closest to rheobase), rheobase, and f-I slope (all five spiking sweeps, up to rheobase $+80 \text{ pA}$). Spike train properties were calculated for each spiking sweep: latency, average firing rate, initial instantaneous firing rate (inverse of first ISI),

mean and median ISI, ISI CV, irregularity ratio, and adaptation index. These spike train features and the single spike properties listed above (measured on the first AP) were summarized for both the rheobase sweep and a stimulus 40pA above rheobase. For spike upstroke, 10 downstroke, width, threshold, and interspike interval (ISI), "adaptation ratio" features were calculated as a ratio of the spike features between the first and third spike (on the lowest amplitude stimulus to elicit at least four spikes). Spike shape properties were also calculated for short (3 ms) pulse stimulation and a slowly increasing current ramp stimulus (first spike only). A subset of cells also had sub-threshold 15 frequency response characterized by a logarithmic chirp stimulus (sine wave with exponentially increasing frequency), for which the impedance profile was calculated and characterized by features including the peak frequency and peak ratio. Feature extraction was implemented using the IPFX python package; custom code used for chirps and some high-level features will be released in a future version of IPFX.

Morphology feature analysis

Prior to morphological feature analysis, reconstructed neuronal morphologies were expanded in the dimension perpendicular to the cut surface to correct for shrinkage (77, 78) after tissue processing. The amount of shrinkage was calculated by comparing the distance of the soma to the cut surface during recording and after fixation and reconstruction. For mouse cells, a tilt angle correction was also performed based on the estimated difference (through CCF registration) between the slicing angle and the direct pia-white matter direction at the cell's location (48). Features predominantly determined by differences in the z-dimension were not analyzed to minimize technical artifacts due to z-compression of the slice after processing.

Morphological features were calculated as previously described (48). In brief, feature definitions were collected from prior studies (79, 80). Features were calculated using the skeleton keys python package (https://github.com/AllenInstitute/skeleton_keys). Features were extracted from neurons aligned in the direction perpendicular to pia and white matter. Laminar axon histograms (bin size of 5 microns) and earth movers distance features require a layer-aligned version of the morphology where node depths are registered to an average laminar depth template.

Statistical analysis of variability

To assess the variability of morphological features within the acute and culture paradigm, we used a Mann-Whitney U test for each condition. Results were reported as the resulting U statistic and the P value. P values were cor-

rected for false discovery rate (FDR, Benjamini-Hochberg procedure). Analysis of feature relationships across subclass were assessed using a one-way ANOVA on ranks (KW, Kruskal-Wallis test), correction for FDR and post-hoc Dunn's tests were run across any pairwise comparison, with an FDR correction when necessary. Analysis of feature relationships with other variables including days in culture and qualitative morphology types were likewise assessed by Mann-Whitney tests for binary variables, KW test for categorical, and Pearson's correlations for continuous variables, FDR-corrected across features when necessary.

Unless otherwise specified, statistical analyses of morphological features were implemented in python using both the statsmodels and scipy packages. Statistical analyses of electrophysiological features were implemented in Prism or python using both the statsmodels and scipy packages.

Morphological Clustering

The co-clustering matrix for the SST and PVALB subclass morphology dataset was calculated by iterative random sampling. During each iteration, 95% of samples were randomly selected to create a shared nearest neighbors graph. We then applied the Fast-greedy community detection algorithm using the Python package python-igraph for clustering assignment. For each pair of samples, the co-clustering score was defined as the times of co-clustering normalized by the iterations of co-occurring. Resampling was performed 500 times to reach saturation. Agglomerative clustering using ward linkage was performed on the co-clustering matrix to get clusters.

Calculating differentially expressed genes

Differentially expressed (DE) genes were calculated for several analyses using the "FindMarkers" function from Seurat V4 (<https://satijalab.org/seurat/>) (81). This function performs either a Wilcoxon test or a t test to calculate a P value and Bonferroni correction to determine whether genes are DE in two groups. This was used to find DE genes in the following cases: (i) culture microglial genes: cultured cells with and without microglia signature (test.use = "wilcox", min.pct = 0.5, logfc.threshold = 4); (ii) generic microglial genes: common genes with and without microglia signature (wilcox, 0.25, 2) in acute and culture cells; (iii) genes increasing or decreasing in PVALB cells in culture: common genes DE in acute versus culture cells (wilcox, 0.25, 2) with and without microglia signature; and (iv) morphology type genes: genes DE between cells with any pair of DBC, MC, and Sparse SST morphologies (t test, 0, 0). Genes DE between dissociated cells in SST and PVALB cell types were calculated using the RNA-seq Data Navigator tool (<https://celltypes.brain-map.org/rnaseq/human/mtg>), by defining

“Set 1 Selection” and “Set 2 Selection” as all PVABL and SST types (excluding SST FRZB) and then running “Find Marker Genes.”

Assigning cells a microglial signature

Microglial signature genes were initially defined in cells from culture by following the standard Seurat pipeline for clustering. First, the top variable genes were defined using FindVariableFeatures Seurat function with default parameters. The data was then scaled (using ScaleData), and the dimensionality was reduced by calculating the first 20 principal components (RunPCA), and then generating a 2D UMAP. Finally, cells were clustered into two clusters by running FindNeighbors on the UMAP space and FindClusters with resolution = 0.001. These clusters were used as initial cell sets to define 269 culture microglial genes, as described above. Final microglial cells were defined by re-running this clustering process independently on cells from culture and cells from acute dissections but using the 269 culture microglial genes as manually input variable genes and setting clustering resolution to 0.1.

Visualization of integrated transcriptomic space

To account for the non-negligible gene expression signatures of culture and microglia, we divided the Patch-seq dataset into four groups (acute, acute - microglial, culture, culture - microglial) and integrated these data together with dissociated reference nuclei by following the Seurat tutorial for integration (8). To do this we applied the “FindIntegrationAnchor” function setting the union of all tree-mapping marker genes as the set of anchor features, with dissociated cells as the reference data set. We then applied IntegrateData using default parameters to put all cells in the same transcriptomic space. We then scaled the data, reduced the dimensionality using principal component analysis (PCA; 30 PCs), and visualized the results with 2D UMAPs. Finally, metadata such as cluster, paradigm, microglial status, and morphology type were then overlaid onto this UMAP space using different colored or shaped points for all or a subset of cells. Except as noted below, all transcriptomics UMAPs are presented in this UMAP space.

The UMAP in figure S1C was generated using a union of the top 50 generic microglial genes, 50 acute cell markers, and 50 culture cell markers as variable genes, and following the above process without using data integration. Likewise, the UMAP in Fig. 4D follows the same procedure only on SST CALB1 neurons, setting the 253 genes DE between 10 DBC, MC, and Sparse SST neurons as variable genes.

REFERENCES AND NOTES

- R. D. Hodge et al., Conserved cell types with divergent features in human versus mouse cortex. *Nature* **573**, 61–68 (2019). doi: [10.1038/s41586-019-1506-7](https://doi.org/10.1038/s41586-019-1506-7); pmid: [31435019](https://pubmed.ncbi.nlm.nih.gov/31435019/)
- T. E. Bakken et al., Comparative cellular analysis of motor cortex in human, marmoset and mouse. *Nature* **598**, 111–119 (2021). doi: [10.1038/s41586-021-03465-8](https://doi.org/10.1038/s41586-021-03465-8); pmid: [34616062](https://pubmed.ncbi.nlm.nih.gov/34616062/)
- E. Boldog et al., Transcriptomic and morphophysiological evidence for a specialized human cortical GABAergic cell type. *Nat. Neurosci.* **21**, 1185–1195 (2018). doi: [10.1038/s41593-018-0205-2](https://doi.org/10.1038/s41593-018-0205-2); pmid: [30150662](https://pubmed.ncbi.nlm.nih.gov/30150662/)
- A. A. Pollen et al., Molecular identity of human outer radial glia during cortical development. *Cell* **163**, 55–67 (2015). doi: [10.1016/j.cell.2015.09.004](https://doi.org/10.1016/j.cell.2015.09.004); pmid: [26406371](https://pubmed.ncbi.nlm.nih.gov/26406371/)
- J. D. Welch et al., Single-Cell Multi-omic Integration Compares and Contrasts Features of Brain Cell Identity. *Cell* **177**, 1873–1887.e17 (2019). doi: [10.1016/j.cell.2019.05.006](https://doi.org/10.1016/j.cell.2019.05.006); pmid: [31178122](https://pubmed.ncbi.nlm.nih.gov/31178122/)
- F. M. Kriener et al., Innovations present in the primate interneuron repertoire. *Nature* **586**, 262–269 (2020). doi: [10.1038/s41586-020-2781-z](https://doi.org/10.1038/s41586-020-2781-z); pmid: [32999462](https://pubmed.ncbi.nlm.nih.gov/32999462/)
- S. Darmanis et al., A survey of human brain transcriptome diversity at the single cell level. *Proc. Natl. Acad. Sci. U.S.A.* **112**, 7285–7290 (2015). doi: [10.1073/pnas.1507125112](https://doi.org/10.1073/pnas.1507125112); pmid: [26060301](https://pubmed.ncbi.nlm.nih.gov/26060301/)
- B. B. Lake et al., Neuronal subtypes and diversity revealed by single-nucleus RNA sequencing of the human brain. *Science* **352**, 1586–1590 (2016). doi: [10.1126/science.aaf1204](https://doi.org/10.1126/science.aaf1204); pmid: [27339989](https://pubmed.ncbi.nlm.nih.gov/27339989/)
- B. B. Lake et al., Integrative single-cell analysis of transcriptional and epigenetic states in the human adult brain. *Nat. Biotechnol.* **36**, 70–80 (2018). doi: [10.1038/nbt.4038](https://doi.org/10.1038/nbt.4038); pmid: [29227469](https://pubmed.ncbi.nlm.nih.gov/29227469/)
- C. Luo et al., Single nucleus multi-omics identifies human cortical cell regulatory genome diversity. *Cell Genomics* **2**, 100107 (2022). doi: [10.1016/j.xgen.2022.100107](https://doi.org/10.1016/j.xgen.2022.100107); pmid: [35419551](https://pubmed.ncbi.nlm.nih.gov/35419551/)
- K. Siletti et al., Transcriptomic diversity of cell types across the adult human brain. *Science* **382**, eadd7046 (2023). doi: [10.1126/science.add7046](https://doi.org/10.1126/science.add7046)
- J. Fuzik et al., Integration of electrophysiological recordings with single-cell RNA-seq data identifies neuronal subtypes. *Nat. Biotechnol.* **34**, 175–183 (2016). doi: [10.1038/nbt.3443](https://doi.org/10.1038/nbt.3443); pmid: [26689544](https://pubmed.ncbi.nlm.nih.gov/26689544/)
- C. R. Cadwell et al., Electrophysiological, transcriptomic and morphologic profiling of single neurons using Patch-seq. *Nat. Biotechnol.* **34**, 199–203 (2016). doi: [10.1038/nbt.3445](https://doi.org/10.1038/nbt.3445); pmid: [26689543](https://pubmed.ncbi.nlm.nih.gov/26689543/)
- B. R. Lee et al., Scaled, high fidelity electrophysiological, morphological, and transcriptomic cell characterization. *eLife* **10**, e65482 (2021). doi: [10.7554/eLife.65482](https://doi.org/10.7554/eLife.65482); pmid: [34378544](https://pubmed.ncbi.nlm.nih.gov/34378544/)
- J. Berg et al., Human neocortical expansion involves glutamatergic neuron diversification. *Nature* **598**, 151–158 (2021). doi: [10.1038/s41586-021-03813-8](https://doi.org/10.1038/s41586-021-03813-8); pmid: [34616067](https://pubmed.ncbi.nlm.nih.gov/34616067/)
- N. W. Gouwens et al., Integrated Morphoelectric and Transcriptomic Classification of Cortical GABAergic Cells. *Cell* **183**, 935–953.e19 (2020). doi: [10.1016/j.cell.2020.09.057](https://doi.org/10.1016/j.cell.2020.09.057); pmid: [33186530](https://pubmed.ncbi.nlm.nih.gov/33186530/)
- F. Scala et al., Phenotypic variation of transcriptomic cell types in mouse motor cortex. *Nature* **598**, 144–150 (2021). doi: [10.1038/s41586-020-2907-3](https://doi.org/10.1038/s41586-020-2907-3); pmid: [33184512](https://pubmed.ncbi.nlm.nih.gov/33184512/)
- B. E. Kalmbach et al., Signature morpho-electric, transcriptomic, and dendritic properties of human layer 5 neocortical pyramidal neurons. *Neuron* **109**, 2914–2927.e5 (2021). doi: [10.1016/j.neuron.2021.08.030](https://doi.org/10.1016/j.neuron.2021.08.030); pmid: [34534454](https://pubmed.ncbi.nlm.nih.gov/34534454/)
- G. Buzsáki, X.-J. Wang, Mechanisms of gamma oscillations. *Annu. Rev. Neurosci.* **35**, 203–225 (2012). doi: [10.1146/annurev-neuro-062111-150444](https://doi.org/10.1146/annurev-neuro-062111-150444); pmid: [22443509](https://pubmed.ncbi.nlm.nih.gov/22443509/)
- E. M. Goldberg, D. A. Coulter, Mechanisms of epileptogenesis: A convergence on neural circuit dysfunction. *Nat. Rev. Neurosci.* **14**, 337–349 (2013). doi: [10.1038/nrn3482](https://doi.org/10.1038/nrn3482); pmid: [23595016](https://pubmed.ncbi.nlm.nih.gov/23595016/)
- D. A. Lewis, Inhibitory neurons in human cortical circuits: Substrate for cognitive dysfunction in schizophrenia. *Curr. Opin. Neurobiol.* **26**, 22–26 (2014). doi: [10.1016/j.conb.2013.11.003](https://doi.org/10.1016/j.conb.2013.11.003); pmid: [24650500](https://pubmed.ncbi.nlm.nih.gov/24650500/)
- O. Marín, Interneuron dysfunction in psychiatric disorders. *Nat. Rev. Neurosci.* **13**, 107–120 (2012). doi: [10.1038/nrn3155](https://doi.org/10.1038/nrn3155); pmid: [22251963](https://pubmed.ncbi.nlm.nih.gov/22251963/)
- H. Zeng, J. R. Sanes, Neuronal cell-type classification: Challenges, opportunities and the path forward. *Nat. Rev. Neurosci.* **18**, 530–546 (2017). doi: [10.1038/nrn.2017.85](https://doi.org/10.1038/nrn.2017.85); pmid: [28757344](https://pubmed.ncbi.nlm.nih.gov/28757344/)
- B. Wamsley, G. Fishell, Genetic and activity-dependent mechanisms underlying interneuron diversity. *Nat. Rev. Neurosci.* **18**, 299–309 (2017). doi: [10.1038/nrn.2017.30](https://doi.org/10.1038/nrn.2017.30); pmid: [28381833](https://pubmed.ncbi.nlm.nih.gov/28381833/)
- B. Tasic et al., Adult mouse cortical cell taxonomy revealed by single cell transcriptomics. *Nat. Neurosci.* **19**, 335–346 (2016). doi: [10.1038/nn.4216](https://doi.org/10.1038/nn.4216); pmid: [26727548](https://pubmed.ncbi.nlm.nih.gov/26727548/)
- B. Tasic et al., Shared and distinct transcriptomic cell types across neocortical areas. *Nature* **563**, 72–78 (2018). doi: [10.1038/s41586-018-0654-5](https://doi.org/10.1038/s41586-018-0654-5); pmid: [30382198](https://pubmed.ncbi.nlm.nih.gov/30382198/)
- B. Wang et al., A Subtype of Inhibitory Interneuron with Intrinsic Persistent Activity in Human and Monkey Neocortex. *Cell Rep.* **10**, 1450–1458 (2015). doi: [10.1016/j.celrep.2015.02.018](https://doi.org/10.1016/j.celrep.2015.02.018); pmid: [25753411](https://pubmed.ncbi.nlm.nih.gov/25753411/)
- C. Varga, G. Tamas, P. Barzo, S. Olah, P. Somogyi, Molecular and Electrophysiological Characterization of GABAergic Interneurons Expressing the Transcription Factor COUP-TFII in the Adult Human Temporal Cortex. *Cereb. Cortex* **25**, 4430–4449 (2015). doi: [10.1093/cercor/bhv045](https://doi.org/10.1093/cercor/bhv045); pmid: [25787832](https://pubmed.ncbi.nlm.nih.gov/25787832/)
- S. Olah et al., Regulation of cortical microcircuits by unitary GABA-mediated volume transmission. *Nature* **461**, 1278–1281 (2009). doi: [10.1038/nature08503](https://doi.org/10.1038/nature08503); pmid: [19865171](https://pubmed.ncbi.nlm.nih.gov/19865171/)
- S. Olah et al., Output of neurogliaform cells to various neuron types in the human and rat cerebral cortex. *Front. Neural Circuits* **1**, 4 (2007). doi: [10.3389/neuro.04.004.2007](https://doi.org/10.3389/neuro.04.004.2007); pmid: [18946546](https://pubmed.ncbi.nlm.nih.gov/18946546/)
- J. Obermayer et al., Lateral inhibition by Martinotti interneurons is facilitated by cholinergic inputs in human and mouse neocortex. *Nat. Commun.* **9**, 4101 (2018). doi: [10.1038/s41467-018-06628-w](https://doi.org/10.1038/s41467-018-06628-w); pmid: [30291244](https://pubmed.ncbi.nlm.nih.gov/30291244/)
- T. Kroon et al., Group I mGluR-Mediated Activation of Martinotti Cells Inhibits Local Cortical Circuitry in Human Cortex. *Front. Cell. Neurosci.* **13**, 315 (2019). doi: [10.3389/fncel.2019.00315](https://doi.org/10.3389/fncel.2019.00315); pmid: [31354435](https://pubmed.ncbi.nlm.nih.gov/31354435/)
- N. Schwarz et al., Long-term adult human brain slice cultures as a model system to study human CNS circuitry and disease. *eLife* **8**, e48417 (2019). doi: [10.7554/eLife.48417](https://doi.org/10.7554/eLife.48417); pmid: [31498083](https://pubmed.ncbi.nlm.nih.gov/31498083/)
- J. T. Ting et al., A robust ex vivo experimental platform for molecular-genetic dissection of adult human neocortical cell types and circuits. *Sci. Rep.* **8**, 8407 (2018). doi: [10.1038/s41598-018-26803-9](https://doi.org/10.1038/s41598-018-26803-9); pmid: [29849137](https://pubmed.ncbi.nlm.nih.gov/29849137/)
- J. K. Mich et al., Functional enhancer elements drive subclass-selective expression from mouse to primate neocortex. *Cell Rep.* **34**, 108754 (2021). doi: [10.1016/j.celrep.2021.108754](https://doi.org/10.1016/j.celrep.2021.108754); pmid: [33789096](https://pubmed.ncbi.nlm.nih.gov/33789096/)
- T. Chartrand et al., Morphoelectric and transcriptomic divergence of the layer 1 interneuron repertoire in human versus mouse neocortex. *Science* **382**, eadf0805 (2023). doi: [10.1126/science.adf0805](https://doi.org/10.1126/science.adf0805)
- K. Arbab, Y. Jiang, D. Howard, W. Inoue, G. Gonzalez-Burgos, D. Felsky, S. J. Tripathy, Investigating microglia-neuron crosstalk by characterizing microglial contamination in human and mouse Patch-seq datasets. *bioRxiv* 2022.09.07.507009 [Preprint] (2022); doi: [10.1101/2022.09.07.507009](https://doi.org/10.1101/2022.09.07.507009)
- Y. Hao et al., Integrated analysis of multimodal single-cell data. *Cell* **184**, 3573–3587.e29 (2021). doi: [10.1016/j.cell.2021.04.048](https://doi.org/10.1016/j.cell.2021.04.048); pmid: [34062119](https://pubmed.ncbi.nlm.nih.gov/34062119/)
- E. Becht et al., Dimensionality reduction for visualizing single-cell data using UMAP. *Nat. Biotechnol.* **37**, 38–44 (2018). doi: [10.1038/nbt.4314](https://doi.org/10.1038/nbt.4314); pmid: [30531897](https://pubmed.ncbi.nlm.nih.gov/30531897/)
- S. J. Tripathy et al., Assessing Transcriptome Quality in Patch-Seq Datasets. *Front. Mol. Neurosci.* **11**, 363 (2018). doi: [10.3389/fnmol.2018.00363](https://doi.org/10.3389/fnmol.2018.00363); pmid: [30349457](https://pubmed.ncbi.nlm.nih.gov/30349457/)
- D. S. Bortone, S. R. Olsen, M. Scanziani, Translaminar inhibitory neurons recruited by layer 6 corticothalamic neurons suppress visual cortex. *Neuron* **82**, 474–485 (2014). doi: [10.1016/j.neuron.2014.02.021](https://doi.org/10.1016/j.neuron.2014.02.021); pmid: [24656931](https://pubmed.ncbi.nlm.nih.gov/24656931/)
- F. Scala et al., Layer 4 of mouse neocortex differs in cell types and circuit organization between sensory areas. *Nat. Commun.* **10**, 4174 (2019). doi: [10.1038/s41467-019-12058-z](https://doi.org/10.1038/s41467-019-12058-z); pmid: [31519874](https://pubmed.ncbi.nlm.nih.gov/31519874/)
- Y. Ma, H. Hu, A. S. Berrebi, P. H. Mathers, A. Agmon, Distinct subtypes of somatostatin-containing neocortical interneurons revealed in transgenic mice. *J. Neurosci.* **26**, 5069–5082 (2006). doi: [10.1523/JNEUROSCI.0661-06.2006](https://doi.org/10.1523/JNEUROSCI.0661-06.2006); pmid: [16687498](https://pubmed.ncbi.nlm.nih.gov/16687498/)
- A. Naka et al., Complementary networks of cortical somatostatin interneurons enforce layer specific control. *eLife* **8**, e43696 (2019). doi: [10.7554/eLife.43696](https://doi.org/10.7554/eLife.43696); pmid: [30883329](https://pubmed.ncbi.nlm.nih.gov/30883329/)
- G. A. Ascoli et al., Petilla terminology: Nomenclature of features of GABAergic interneurons of the cerebral cortex. *Nat. Rev. Neurosci.* **9**, 557–568 (2008). doi: [10.1038/nrn2402](https://doi.org/10.1038/nrn2402); pmid: [18568015](https://pubmed.ncbi.nlm.nih.gov/18568015/)
- Q. Xu, I. Cobos, E. De La Cruz, J. L. Rubenstein, S. A. Anderson, Origins of cortical interneuron subtypes. *J. Neurosci.* **24**, 2612–2622 (2004). doi: [10.1523/JNEUROSCI.5667-03.2004](https://doi.org/10.1523/JNEUROSCI.5667-03.2004); pmid: [15028753](https://pubmed.ncbi.nlm.nih.gov/15028753/)

47. B. Wang *et al.*, Firing Frequency Maxima of Fast-Spiking Neurons in Human, Monkey, and Mouse Neocortex. *Front. Cell. Neurosci.* **10**, 239 (2016). doi: [10.3389/fncel.2016.00239](https://doi.org/10.3389/fncel.2016.00239); pmid: [27803650](https://pubmed.ncbi.nlm.nih.gov/27803650/)
48. N. W. Gouwens *et al.*, Classification of electrophysiological and morphological neuron types in the mouse visual cortex. *Nat. Neurosci.* **22**, 1182–1195 (2019). doi: [10.1038/s41593-019-0417-0](https://doi.org/10.1038/s41593-019-0417-0); pmid: [31209381](https://pubmed.ncbi.nlm.nih.gov/31209381/)
49. J. DeFelipe *et al.*, New insights into the classification and nomenclature of cortical GABAergic interneurons. *Nat. Rev. Neurosci.* **14**, 202–216 (2013). doi: [10.1038/nrn3444](https://doi.org/10.1038/nrn3444); pmid: [23385869](https://pubmed.ncbi.nlm.nih.gov/23385869/)
50. J. DeFelipe, S. H. C. Hendry, E. G. Jones, A correlative electron microscopic study of basket cells and large GABAergic neurons in the monkey sensory-motor cortex. *Neuroscience* **17**, 991–1009 (1986). doi: [10.1016/0306-4522\(86\)90075-8](https://doi.org/10.1016/0306-4522(86)90075-8); pmid: [2423922](https://pubmed.ncbi.nlm.nih.gov/2423922/)
51. J. DeFelipe, M. C. González-Albo, M. R. Del Rio, G. N. Elston, Distribution and patterns of connectivity of interneurons containing calbindin, calretinin, and parvalbumin in visual areas of the occipital and temporal lobes of the macaque monkey. *J. Comp. Neurol.* **412**, 515–526 (1999). doi: [10.1002/\(SICI\)1096-9861\(19990927\)412:3<515::AID-CNE10>3.0.CO;2-1](https://doi.org/10.1002/(SICI)1096-9861(19990927)412:3<515::AID-CNE10>3.0.CO;2-1); pmid: [10441237](https://pubmed.ncbi.nlm.nih.gov/10441237/)
52. G. Tamás, E. H. Buhl, P. Somogyi, Massive autaptic self-innervation of GABAergic neurons in cat visual cortex. *J. Neurosci.* **17**, 6352–6364 (1997). doi: [10.1523/JNEUROSCI.17-16-06352.1997](https://doi.org/10.1523/JNEUROSCI.17-16-06352.1997); pmid: [9236244](https://pubmed.ncbi.nlm.nih.gov/9236244/)
53. G. Tamás, P. Somogyi, E. H. Buhl, Differentially interconnected networks of GABAergic interneurons in the visual cortex of the cat. *J. Neurosci.* **18**, 4255–4270 (1998). doi: [10.1523/JNEUROSCI.18-11-04256.1998](https://doi.org/10.1523/JNEUROSCI.18-11-04256.1998); pmid: [9592103](https://pubmed.ncbi.nlm.nih.gov/9592103/)
54. I. B. Yáñez *et al.*, Double bouquet cell in the human cerebral cortex and a comparison with other mammals. *J. Comp. Neurol.* **486**, 344–360 (2005). doi: [10.1002/cne.20533](https://doi.org/10.1002/cne.20533); pmid: [15846784](https://pubmed.ncbi.nlm.nih.gov/15846784/)
55. J. DeFelipe, I. Ballesteros-Yáñez, M. C. Inda, A. Muñoz, "Double-bouquet cells in the monkey and human cerebral cortex with special reference to areas 17 and 18" in *Progress in Brain Research* (Elsevier, 2006) vol. 154, pp. 15–32.
56. I. P. Lukacs *et al.*, Differential effects of group III metabotropic glutamate receptors on spontaneous inhibitory synaptic currents in spine-innervating double bouquet and parvalbumin-expressing dendrite-targeting GABAergic interneurons in human neocortex. *bioRxiv* 2022.03.05.483105 [Preprint] (2022); <https://doi.org/10.1101/2022.03.05.483105>.
57. B. E. Kalmbach *et al.*, h-Channels Contribute to Divergent Intrinsic Membrane Properties of Supragranular Pyramidal Neurons in Human versus Mouse Cerebral Cortex. *Neuron* **100**, 1194–1208.e5 (2018). doi: [10.1016/j.neuron.2018.10.012](https://doi.org/10.1016/j.neuron.2018.10.012); pmid: [30392798](https://pubmed.ncbi.nlm.nih.gov/30392798/)
58. V. Szegedi *et al.*, HCN channels at the cell soma ensure the rapid electrical reactivity of fast-spiking interneurons in human neocortex. *PLOS Biol.* **21**, e3002001 (2023). doi: [10.1371/journal.pbio.3002001](https://doi.org/10.1371/journal.pbio.3002001); pmid: [36745683](https://pubmed.ncbi.nlm.nih.gov/36745683/)
59. N. P. Poolos, M. Migliore, D. Johnston, Pharmacological upregulation of h-channels reduces the excitability of pyramidal neuron dendrites. *Nat. Neurosci.* **5**, 767–774 (2002). doi: [10.1038/nrn891](https://doi.org/10.1038/nrn891); pmid: [12118259](https://pubmed.ncbi.nlm.nih.gov/12118259/)
60. H. Zeng *et al.*, Large-scale cellular-resolution gene profiling in human neocortex reveals species-specific molecular signatures. *Cell* **149**, 483–496 (2012). doi: [10.1016/j.cell.2012.02.052](https://doi.org/10.1016/j.cell.2012.02.052); pmid: [22500809](https://pubmed.ncbi.nlm.nih.gov/22500809/)
61. X. Wang *et al.*, Genetic Single Neuron Anatomy Reveals Fine Granularity of Cortical Axo-Axonic Cells. *Cell Rep.* **26**, 3145–3159.e5 (2019). doi: [10.1016/j.celrep.2019.02.040](https://doi.org/10.1016/j.celrep.2019.02.040); pmid: [30865900](https://pubmed.ncbi.nlm.nih.gov/30865900/)
62. Z. Yao *et al.*, A taxonomy of transcriptomic cell types across the isocortex and hippocampal formation. *Cell* **184**, 3222–3241.e26 (2021). doi: [10.1016/j.cell.2021.04.021](https://doi.org/10.1016/j.cell.2021.04.021); pmid: [3404146](https://pubmed.ncbi.nlm.nih.gov/3404146/)
63. H. Liu *et al.*, DNA methylation atlas of the mouse brain at single-cell resolution. *Nature* **598**, 120–128 (2021). doi: [10.1038/s41586-020-03182-8](https://doi.org/10.1038/s41586-020-03182-8); pmid: [34616061](https://pubmed.ncbi.nlm.nih.gov/34616061/)
64. Z. Zhang *et al.*, Epigenomic diversity of cortical projection neurons in the mouse brain. *Nature* **598**, 167–173 (2021). doi: [10.1038/s41586-021-03223-w](https://doi.org/10.1038/s41586-021-03223-w); pmid: [34616065](https://pubmed.ncbi.nlm.nih.gov/34616065/)
65. Y. E. Li *et al.*, An atlas of gene regulatory elements in adult mouse cerebrum. *Nature* **598**, 129–136 (2021). doi: [10.1038/s41586-021-03604-1](https://doi.org/10.1038/s41586-021-03604-1); pmid: [34616068](https://pubmed.ncbi.nlm.nih.gov/34616068/)
66. L. T. Graybuck *et al.*, Enhancer viruses for combinatorial cell-subclass-specific labeling. *Neuron* **109**, 1449–1464.e13 (2021). doi: [10.1016/j.neuron.2021.03.011](https://doi.org/10.1016/j.neuron.2021.03.011); pmid: [33789083](https://pubmed.ncbi.nlm.nih.gov/33789083/)
67. S. Hrvatin *et al.*, A scalable platform for the development of cell-type-specific viral drivers. *eLife* **8**, e48089 (2019). doi: [10.7554/eLife.48089](https://doi.org/10.7554/eLife.48089); pmid: [31545165](https://pubmed.ncbi.nlm.nih.gov/31545165/)
68. D. Vormstein-Schneider *et al.*, Viral manipulation of functionally distinct interneurons in mice, non-human primates and humans. *Nat. Neurosci.* **23**, 1629–1636 (2020). doi: [10.1038/s41593-020-0692-9](https://doi.org/10.1038/s41593-020-0692-9); pmid: [32807948](https://pubmed.ncbi.nlm.nih.gov/32807948/)
69. J. T. Ting, T. L. Daigle, Q. Chen, G. Feng, "Acute Brain Slice Methods for Adult and Aging Animals: Application of Targeted Patch Clamp Analysis and Optogenetics" in *Patch-Clamp Methods and Protocols*, M. Martina, S. Taverna, Eds. (Springer, 2014), *Methods in Molecular Biology*, pp. 221–242. doi: [10.1007/978-1-4939-1096-0_14](https://doi.org/10.1007/978-1-4939-1096-0_14)
70. T. Zerucha *et al.*, A highly conserved enhancer in the Dlx5/Dlx6 intergenic region is the site of cross-regulatory interactions between Dlx genes in the embryonic forebrain. *J. Neurosci.* **20**, 709–721 (2000). doi: [10.1523/JNEUROSCI.20-02-00709.2000](https://doi.org/10.1523/JNEUROSCI.20-02-00709.2000); pmid: [10632600](https://pubmed.ncbi.nlm.nih.gov/10632600/)
71. A. Dobin *et al.*, STAR: Ultrafast universal RNA-seq aligner. *Bioinformatics* **29**, 15–21 (2013). doi: [10.1093/bioinformatics/bts635](https://doi.org/10.1093/bioinformatics/bts635); pmid: [23104886](https://pubmed.ncbi.nlm.nih.gov/23104886/)
72. M. Lawrence *et al.*, Software for computing and annotating genomic ranges. *PLOS Comput. Biol.* **9**, e1003118 (2013). doi: [10.1371/journal.pcbi.1003118](https://doi.org/10.1371/journal.pcbi.1003118); pmid: [23950696](https://pubmed.ncbi.nlm.nih.gov/23950696/)
73. V. S. Fonov, A. C. Evans, R. C. McKinstry, C. R. Almlöf, D. L. Collins, Unbiased nonlinear average age-appropriate brain templates from birth to adulthood. *Neuroimage* **47**, SI02 (2009). doi: [10.1016/S1053-8119\(09\)70884-5](https://doi.org/10.1016/S1053-8119(09)70884-5)
74. S.-L. Ding *et al.*, Comprehensive cellular-resolution atlas of the adult human brain. *J. Comp. Neurol.* **524**, 3127–3481 (2016). doi: [10.1002/cne.24080](https://doi.org/10.1002/cne.24080); pmid: [27418273](https://pubmed.ncbi.nlm.nih.gov/27418273/)
75. H. Peng, A. Bria, Z. Zhou, G. Iannello, F. Long, Extensible visualization and analysis for multidimensional images using Vaa3D. *Nat. Protoc.* **9**, 193–208 (2014). doi: [10.1038/nprot.2014.011](https://doi.org/10.1038/nprot.2014.011); pmid: [24385149](https://pubmed.ncbi.nlm.nih.gov/24385149/)
76. A. Bria, G. Iannello, L. Onofri, H. Peng, TeraFly: Real-time three-dimensional visualization and annotation of terabytes of multidimensional volumetric images. *Nat. Methods* **13**, 192–194 (2016). doi: [10.1038/nmeth.3767](https://doi.org/10.1038/nmeth.3767); pmid: [26914202](https://pubmed.ncbi.nlm.nih.gov/26914202/)
77. V. Egger, T. Nevian, R. M. Bruno, Subcolumnar dendritic and axonal organization of spiny stellate and star pyramid neurons within a barrel in rat somatosensory cortex. *Cereb. Cortex* **18**, 876–889 (2008). doi: [10.1093/cercor/bhm126](https://doi.org/10.1093/cercor/bhm126); pmid: [18756622](https://pubmed.ncbi.nlm.nih.gov/18756622/)
78. Y. Deitrich *et al.*, Comprehensive Morpho-Electrotomographic Analysis Shows 2 Distinct Classes of L2 and L3 Pyramidal Neurons in Human Temporal Cortex. *Cereb. Cortex* **27**, 5398–5414 (2017). doi: [10.1093/cercor/bhw226](https://doi.org/10.1093/cercor/bhw226); pmid: [28968789](https://pubmed.ncbi.nlm.nih.gov/28968789/)
79. R. Scorcioni, S. Polavaram, G. A. Ascoli, L-Measure: A web-accessible tool for the analysis, comparison and search of digital reconstructions of neuronal morphologies. *Nat. Protoc.* **3**, 866–876 (2008). doi: [10.1038/nprot.2008.51](https://doi.org/10.1038/nprot.2008.51); pmid: [18451794](https://pubmed.ncbi.nlm.nih.gov/18451794/)
80. H. Markram *et al.*, Reconstruction and Simulation of Neocortical Microcircuitry. *Cell* **163**, 456–492 (2015). doi: [10.1016/j.cell.2015.09.029](https://doi.org/10.1016/j.cell.2015.09.029); pmid: [26451489](https://pubmed.ncbi.nlm.nih.gov/26451489/)
81. T. Stuart *et al.*, Comprehensive Integration of Single-Cell Data. *Cell* **177**, 1888–1902.e21 (2019). doi: [10.1016/j.cell.2019.05.031](https://doi.org/10.1016/j.cell.2019.05.031); pmid: [31178118](https://pubmed.ncbi.nlm.nih.gov/31178118/)

ACKNOWLEDGMENTS

We thank the Allen Institute founder, P. G. Allen, for his vision, encouragement, and support. We additionally acknowledge support and input from our remaining U01 BRAIN grant consortium colleagues as well as various Allen Institute teams including Tissue Procurement and Tissue Processing, Viral Technology, Neuroanatomy, Histology and Reagent Prep, Imaging, Rseq core, Molecular Genetics, Program Management, Human Cell Types, In Vitro Single Cell Characterization, Data and Technology, Engineering, Transcriptomics, and Genomics. We also thank our Seattle-, Amsterdam-, and Szeged-area hospital partners for support and assistance with neurosurgical tissue procurement. This publication was supported by and coordinated through the BICCN. This publication is part of the Human Cell Atlas (www.humancellatlas.org/publications/). **Funding:** The research reported in this publication was supported by the National Institute of Mental Health (NIMH) of the National Institutes of Health (NIH) BRAIN Initiative awards 1RF1MH114126 and 1UG3MH120095 (J.T.T., B.P.L., and E.S.L.), BRAIN Initiative Cell Census Network award U01MH114812 (E.S.L., H.D.M., and G.T.), and by NIMH award 1RF1MH128778 (S.A.S.). The content is solely the responsibility of the authors and does not necessarily represent the official views of the NIH. This work was also supported in part by The Nancy and Buster Alvord Endowment (C.D.K.); grant 945539 (Human Brain Project SGA3) from the European Union's Horizon 2020 Framework Programme for Research and Innovation (H.D.M.); European Research Council advanced grant "fasthumanneuron" 101093198 (H.D.M.); the Dutch Research Council (NWO) Open Competition (ENW-M2) grant OCENW-M20285 (C.P.J.D.K.); the NWO Gravitation program BRAINSCAPES: A Roadmap from Neurogenetics to Neurobiology (NWO: 024.004.012); VI.Vidi.213.014 grant from the Dutch Research Council (N.A.G.); the Danish Cancer Society grants R304-A17698-B5570 and R295-A16770 (A.R.K.); The Lundbeck Foundation grant R325-2019-1490 (A.R.K. and A.O.); the Independent Research Fund Denmark grants 9039-00307B (A.R.K.) and DFF-37741 (W.H.H.); and National Research, Development, and Innovation Office grants KKP 133807 Élvonal, ÚNKP-20-5-SZTE-681, TKP2021-EA-09, TKP-2021-EGA-28, and 2019-21.7-ERA-NET-2022-00038; and Eötvös Loránd Research Network grants ELKH-SZTE Agykérki Neuronhálózatok Kutatócsoport and KÖ-36/2021 (G.T.).

Author contributions: Conceptualization: B.R.L., R.D., B.K., S.A.S., M.C., E.S.L., and J.T.T.; Data curation: B.R.L., R.D., J.A.M., T.Ch., J.C., R.M., A.M., L.N., E.J.M., J.N., L.P., C.D.K., K.S., J.W., A.O., W.H.H., and K.M.; Formal analysis: B.R.L., R.D., J.A.M., T.C., R.M., A.M., S.W.B., L.N., N.Joh., N.Jor., N.W., T.B., N.W.G., A.O., and W.H.H.; Funding acquisition: A.R.K., A.O., M.C., W.H.H., C.D.K., B.P.L., N.A.G., H.D.M., S.A.S., G.T., E.S.L., and J.T.T.; Investigation: B.R.L., R.D., J.A.M., T.Ch., J.C., R.M., A.M., L.N., D.B., K.Br., T.Ca., N.D., M.K., B.L., D.M., G.M., X.O., A.O., A.Po., L.P., R.R., A.R., I.S., M.T., J.T., S.V., F.W., N.W., G.W., J.Wi., R.H., and J.T.T.; Methodology: B.R.L., R.D., J.A.M., J.C., R.M., A.M., L.N., D.B., K.Br., T.Ca., N.D., M.N., X.O., N.T., N.W., S.Y., P.B., C.C., R.G.E., M.F., N.W.G., B.G., R.P.G., J.S.H., C.D.K., A.L.K., J.G.O., A.P., J.R., D.L.S., K.S., J.Wa., E.S.L., J.T.T., M.C., J.C.H.S., and A.R.K.; Project administration: B.R.L., R.D., E.J.M., J.N., S.M.S., B.T., D.V., L.E., K.S., J.W., J.B., N.A.G., B.K., C.P.J.D.K., L.Kr., H.D.M., S.A.S., G.T., E.S.L., J.T.T., M.C., J.C.H.S., and A.R.K.; Resources: B.R.L., R.D., N.D., E.J.M., M.T.M., D.N., X.O., N.T., N.W., S.Y., P.B., C.C., R.G.E., M.F., N.W.G., B.G., R.P.G., J.S.H., C.D.K., A.L.K., J.G.O., A.P., J.R., D.L.S., K.S., J.Wa., E.S.L., J.T.T., M.C., J.C.H.S., and A.R.K.; Software: T.Ch., M.Ma., N.W.G., and T.J.; Supervision: B.R.L., R.D., J.C., N.D., M.Mc., D.M., L.P., S.Y., T.B., T.J., K.S., J.Wa., H.Z., J.B., N.A.G., B.K., C.P.J.D.K., H.D.M., S.A.S., G.T., E.S.L., J.T.T., M.C., and A.R.K.; Visualization: B.R.L., R.D., J.A.M., T.Ch., J.C., R.M., A.M., L.N., N.Joh., N.Jor., M.Ma., N.W.G., A.O., and W.H.H.; Writing – original draft: B.R.L., R.D., J.A.M., and J.T.T.; Writing – review and editing: B.R.L., R.D., J.A.M., T.Ch., A.O., B.K., C.P.J.D.K., H.D.M., S.A.S., G.T., E.S.L., and J.T.T. **Competing interests:** Authors J.T.T., B.P.L., and E.S.L. are listed as inventors on international patent application PCT/US2019/054539, "Artificial expression constructs for selectively modulating gene expression in interneurons." Authors J.T.T., B.P.L., H.Z., and E.S.L. are listed as inventors on international patent application PCT/US2021/036028, "Artificial expression constructs for selectively modulating gene expression in inhibitory neocortical neurons." **Data and materials availability:** All data from the study will be made available through BIL, DANDI, and NeMO repositories. Morphology reconstructions are available at the Brain Image Library (BIL) at <https://doi.org/10.35077/g.892>. Materials related to this manuscript can be found at https://github.com/AllenInstitute/human_patchseq_gaba. Other software libraries essential to the analysis are publicly available at <https://github.com/AllenInstitute/patchseqtools> (Patch-seq), <https://github.com/AllenInstitute/pfx> (electrophysiology), https://github.com/AllenInstitute/neuron_morphology and https://github.com/AllenInstitute/skeleton_keys (morphology), and <https://github.com/AllenInstitute/scratch> (transcriptomics). **License information:** Copyright © 2023 the authors, some rights reserved; exclusive licensee American Association for the Advancement of Science. No claim to original US government works. <https://www.science.org/about/science-licenses-journal-article-reuse>

SUPPLEMENTARY MATERIALS

[sciencescience.org/doi/10.1126/adf6484](https://science.org/doi/10.1126/adf6484)

Figs. S1 to S9

Data S1 and S2

MDAR Reproducibility Checklist

Submitted 9 November 2022; accepted 8 September 2023
10.1126/science.adf6484